

- 1
- 2
- 3
- 4
- 5
- 6
- 7
- 8
- 9
- 10
- 11
- 12
- 13
- 14
- 15
- 16
- 17
- 18
- 19
- 20
- 21
- 22

4

5

6
7

8

9
10
11

12

13

14

15

- 16
17
18
19
20
21

23 **Abstract**

24 Based on the brightness temperature observed by the Fengyun-4A satellite, around
25 eight hundred mesoscale convective systems (MCSs) are identified in the middle
26 reaches of the Yangtze River Basin during the warm seasons (April–September) of
27 2018–2021, which are categorized into the quasistationary (QS) type and the
28 outward-moving (OM; i.e., vacating the source region) type. Afterward, the initiations
29 of the MCSs are backward tracked using a hybrid method of areal overlapping and
30 optical flow. Then, the main features of QS and OM MCSs and their respective
31 synoptic circulations and environmental parameters are analyzed. The QS MCSs
32 primarily occur in July and August and are mainly initiated in the afternoon. The OM
33 MCSs mostly occur in June and July with two initiation peaks appeared at noon and late
34 night, respectively. The QS MCSs are mainly initiated in mountainous areas, and they
35 are primarily caused by local thermal effects. In contrast, the OM MCSs are mainly
36 initiated in plain areas under synoptic forcings. Circulations of a total of 285 days
37 (without direct influencings from tropical cyclones) are objectively classified into three
38 patterns by using the k-means algorithm. Pattern-I (128 days) which is closely related
39 to low-level jets, shows the most similar features to those of typical Mei-yu fronts, and
40 it acts as the most favorable circulation type for MCSs' initiations. Pattern-II (66 days)
41 is dominated by northwesterlies, with a relatively stable layer in the low-level
42 troposphere. Pattern-III (91 days) features a dry-adiabatic or even a superadiabatic
43 layer that contributes to lowering the layer stability.

44 **Plain Language Summary**

45 Mesoscale convective systems (MCSs) often cause severe convective weather over
46 the middle reaches of the Yangtze River Basin and pose a great threat to life and
47 property in this region. This study identified and tracked MCSs using satellite data
48 and categorized them into the quasistationary (QS) type and the outward-moving (OM)
49 type based on their movement features. The QS type primarily occurs in July and
50 August and is mainly initiated in the afternoon over mountains, caused by local thermal
51 effects. The OM type mostly occurs in June and July and is mainly initiated at noon and
52 late night over the plains, which is related to large-scale circulation. Large-scale
53 circulation regulates environmental conditions and further affects the initiation of
54 MCSs. Circulations over the middle reaches of the Yangtze River Basin are classified

into three patterns, each of which is dominated by a large-scale weather system. The circulation pattern dominated by the Mei-yu front is the most favorable for MCS initiation. The circulation pattern dominated by the northwesterly is favorable for the initiation of OM MCSs but not for QS MCSs. The circulation pattern dominated by the southerly produces a strong thermal effect and is favorable for the initiation of QS MCSs.

1 Introduction

Severe convective weather phenomena, such as heavy rainfall, hailstorms, wind gusts and tornadoes, are mainly associated with mesoscale convective systems (MCSs) (Houze, 2004; Maddox, 1980; Zheng et al., 2013). The generalized concept of the MCS usually covers a broad spectrum of temporal and spatial scales (Yang et al., 2015), and MCSs exhibit different forms if different techniques of detection and identification are employed. In conventional weather maps, MCSs are generally presented as mesoscale high/low pressures (Zipser, 1977). Based on precipitation observations, MCSs often appear as mesoscale rain clusters or belts (Shen et al., 2020). However, MCSs usually appear as different radar reflectivity morphologies (Gallus et al., 2008; Ma et al., 2021a; Yang & Sun, 2018). On satellite infrared images, MCSs often appear as cold-cloud shields (CCSs) with a certain temporal and spatial scale (Laing & Fritsch, 1997; Machado et al., 1998; Meng et al., 2021; Yang et al., 2015; Zheng et al., 2008).

Using the criteria of brightness temperature and cloud area, Maddox (1980) detected a kind of meso- α scale convective system, which was later known as the mesoscale convective complex (MCC), and since then, the method based on the criteria of brightness temperature and cloud area has been widely used in research on MCCs (Laing & Fritsch, 1997; Miller & Fritsch, 1991; Rodgers et al., 1983; Velasco & Fritsch, 1987). Augustine and Howard (1988) simplified the method of Maddox (1980) and found that applying the criteria of brightness temperature $\leq -52^{\circ}\text{C}$ and cloud area $\geq 5 \times 10^4 \text{ km}^2$ could better describe the evolution of storms. In recent years, -52°C has been used as the brightness temperature criterion to identify MCSs (Kukulies et al., 2021; Morake et al., 2021; Yang et al., 2015; Yang et al., 2020; Meng et al., 2021), and different cloud area and duration criteria have been applied to determine the spatial and temporal scales of MCSs.

Williams and Houze (1987) developed an algorithm to track an individual cloud

87 cluster in two successive infrared images by calculating the overlapping rate of the two
88 cloud areas, and since then, the areal overlapping method has been widely used in MCS
89 tracking. Morel and Senesi (2002) improved the accuracy of MCS tracking by
90 estimating the movement of clouds and developed the ISIS (instrument de suivi dans
91 l'imagerie satellitaire) algorithm. Feng et al. (2018) improved the tracking accuracy by
92 expanding the area of the target cloud and developed the FLEXTRKR (flexible object
93 tracker) algorithm. In addition, the optical flow approach has been widely used since it
94 was introduced into meteorology research, including the nowcasting of precipitation
95 (Bowler et al., 2004; Bechini & Chandrasekar, 2017; Bowler et al., 2004) and the
96 improvement of numerical forecast results (Marzban & Sandgathe, 2010). In recent
97 years, the optical flow approach has been applied in the research of new generation
98 geostationary satellite products. Vandal and Nemani (2020) improved the temporal
99 resolution of 10.8 μm infrared longwave radiation products of the new generation
100 Geostationary Operational Environmental Satellite from 15 min to 1 min using the
101 optical flow approach, and they successfully captured the evolution of a severe
102 convective event. Burton et al. (2022) applied the optical flow approach to
103 satellite-retrieved rainfall rate products for West Africa, and extrapolations showed
104 useful skill at up to 4 h of lead time. In the present study, the areal overlapping method
105 is used to track MCSs, and the optical flow is calculated to help improve accuracy.

106 Previous studies have mainly focused on the process from the formation to the
107 termination of an MCS. Due to the data resolution and technical method limitations,
108 few studies have focused on the initiation of an MCS. Roberts and Rutledge (2003)
109 suggested that the precursor signal of convection initiation (CI) can be captured on
110 satellites. Subsequently, two algorithms for identifying precursor signals and predicting
111 CI based on satellite observations were developed, namely, the SATCAST (satellite
112 convection analysis and tracking algorithm) algorithm (Mecikalski & Bedka, 2006) and
113 the UWCI (University of Wisconsin Convective Initiation) algorithm (Sieglaff et al.,
114 2011). Both scientific research and operational practice have shown that the initiation
115 of MCSs can be identified through satellite observations.

116 As mentioned above, MCSs have a wide spectrum of spatial and temporal scales,
117 and the features of MCSs, such as the cloud extent, cloud top temperature and cloud
118 motion, vary worldwide (Feng et al., 2019; Kolios & Feidas, 2010; Morel & Senesi,
119 2002; Punkka & Bister, 2015; Rehbein et al., 2018). The activities of MCSs in China

120 have regional characteristics: the highest frequency of MCSs over the Tibetan Plateau
121 occurs in July (Zhang et al., 2021; Jiang & Fan, 2002; Mai et al., 2020) and formed
122 mainly in the afternoon (Zheng et al., 2008); the activities of MCSs in the North China
123 Plain are the most frequent in June, July and August, and the formations occur mostly
124 around noon (Ma et al., 2021a); under the influence of sea–land breeze, the MCSs in
125 South China propagate offshore (inland) at night (in the daytime) (Bai et al., 2020;
126 Zheng et al., 2008).

127 The initiation, development, and organization of MCSs are controlled and
128 regulated by synoptic and mesoscale circulations. Lewis and Gray (2010) found that
129 MCSs in Britain are mainly affected by three types of circulations and that the
130 organization of MCSs is related to the interaction of perturbations at the upper level and
131 warm advections at the lower level. Peters and Schumacher (2014) divided the
132 circulations favorable for MCSs in the Great Plains of the United States into warm
133 season-type and synoptic-type circulations. The synoptic-type MCSs tended to occur
134 downstream of a progressive upper-level trough along a low-level potential
135 temperature gradient with the warmest air to the south and southeast.
136 Warm-season-type MCSs typically occurred within the right-entrance of a minimally to
137 anticyclonically curved upper-level jet along a low-level potential temperature gradient
138 with the warmest air to the southwest. Song et al. (2019) found that the favorable
139 environments for MCSs over the Great Plains of the United States have frontal
140 characteristics and enhanced low-level jets, while the unfavorable environments feature
141 enhanced upper-level ridges. Sugimoto and Ueno (2010) found that MCSs over the
142 eastern Tibetan Plateau mainly occurred under the condition of the eastward extension
143 of the upper tropospheric anticyclone with the enhancement of near-surface low
144 pressure in the western plateau. He et al. (2017) classified the circulation patterns over
145 central East China into nine typical types based on the geopotential height fields at 850
146 hPa, and MCSs mainly occurred in the meridional circulations, which were associated
147 with the Western North Pacific Subtropical High to the east and a low-pressure system
148 to the west.

149 The aforementioned studies show that different synoptic circulations often lead to
150 different environmental conditions, and the interactions of environmental conditions,
151 topography, underlying surface and other factors are highly nonlinear, which makes it
152 difficult to forecast the initiation and development of MCSs. Previous studies involving

the MCS life cycle are still limited in terms of understanding its formation. At present, thanks to high spatial-temporal resolution satellite data, the development of an MCS from initiation to formation can be accurately captured through backward tracking. The middle reaches of the Yangtze River Basin (YRB) are located in the transitional zone between the second-step terrain (mountains) and the plains over East China, with complicated orography and various underlying surfaces. The Mei-yu fronts are very active in this area, and their precipitation and convection have unique characteristics and complicated mechanisms (Fu et al., 2011b; Sun & Zhang, 2012; Zhang et al., 2014, 2020; Wang et al., 2021). In the present study, the MCSs over the middle reaches of the YRB are identified and tracked first, and then, the MCS initiation is detected through backward tracking. Next, the temporal-spatial distribution and features of the MCSs are investigated. Finally, the synoptic circulations in this region are objectively classified into different patterns to find the circulations and environmental conditions favorable for the initiation of an MCS. The remainder of this paper is organized as follows. Section 2 introduces the data and methodologies. Section 3 presents the statistics of MCSs, including the temporal-spatial distributions of initiation and apparent features during their life cycles. Section 4 presents the objective classification of circulations in the middle reaches of the YRB and examines the circulation patterns and environmental conditions favorable for MCS initiation. Finally, a summary is given in Section 5.

2 Data and methodology

2.1 Data and focused area

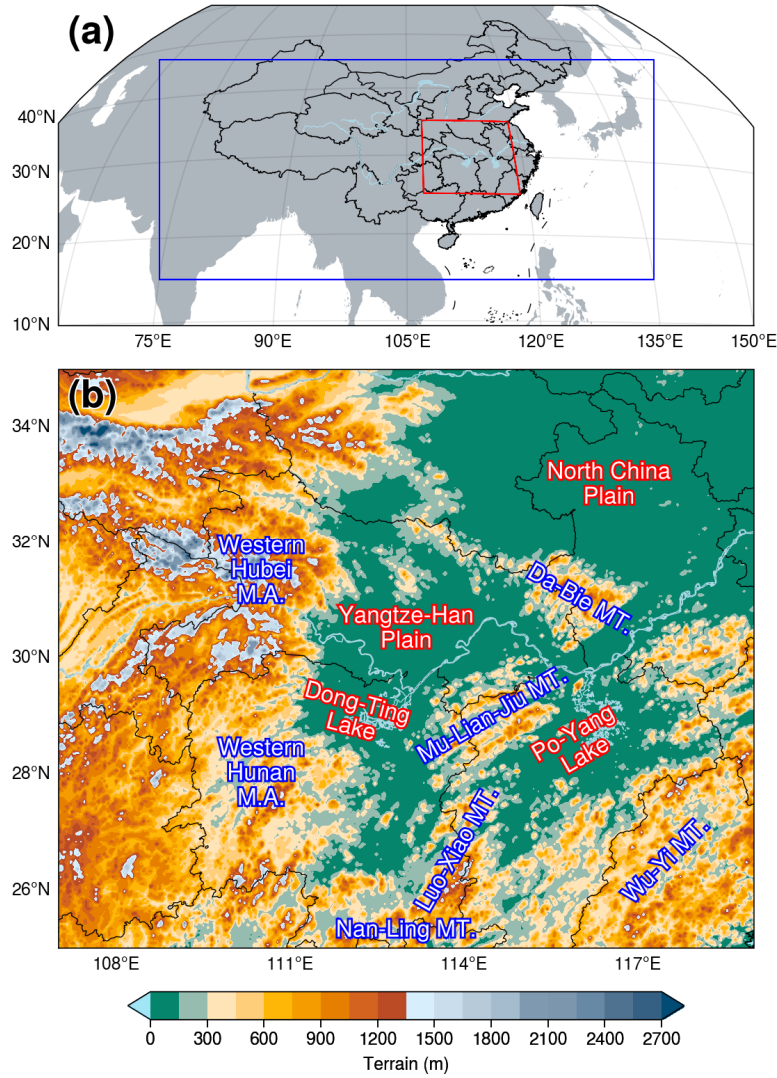
The brightness temperature (BT) at the 10.8 μm band of the Advanced Geosynchronous Radiation Imager onboard the Fengyun-4A (FY-4A) satellite is used to identify and track MCSs in the present study. The spatial resolution of FY-4A BT data is 4 km at nadir. The temporal resolution of regional observations over China and its surrounding area is ~ 5 min (Yang et al., 2017). The BT fields used in the present study are limited to the region ($\sim 15\text{--}45^\circ\text{N}$ and $75\text{--}135^\circ\text{E}$) shown in Fig. 1a to ensure consistency in the dataset. The integrities of the dataset during the warm season (April–September) of 2018–2021 are 93.26%, 97.65%, 97.07%, and 98.05%, respectively, with an average integrity of 94.51%.

Considering that the mechanisms of the convection related to tropical cyclones

185 (TCs) are different from those of extratropical convection (Bister, 2001; Hendricks &
186 Montgomery, 2006; Rodgers et al., 1991), MCSs induced by TCs and circulations
187 related to TCs are excluded using the TC best-track dataset provided by the China
188 Meteorological Administration, and the temporal resolution is 3 h (Lu et al., 2021; Ying
189 et al., 2014).

190 The fifth-generation ECMWF (European Centre for Medium Range Forecasts)
191 reanalysis (ERA5) data, with a temporal resolution of 1 h and a spatial resolution of
192 0.25° (Hersbach et al., 2020), are used in the classification and composite analysis of
193 circulations. The construction of proximity soundings is mainly based on ERA5 data.
194 However, considering the differences in the boundary layer variables between
195 reanalysis and observed soundings (Gensini et al., 2014; King & Kennedy, 2019),
196 correcting the boundary layer variables of the reanalysis sounding is necessary.
197 Therefore, the present study uses the 1-h observations of automatic weather stations
198 (AWSs) provided by the China Meteorological Administration to correct the surface
199 level of the ERA5 data before constructing proximity soundings.

200 The middle reaches of the YRB are defined as the region covering $107\text{--}119^{\circ}\text{E}$ and
201 $25\text{--}35^{\circ}\text{N}$ in the present study (Fig. 1a), and the orography (Fig. 1b) in this area is
202 complicated. The western Hubei mountainous areas and western Hunan mountainous
203 areas are located in the west, the Nan-Ling Mountains are in the south and the Wu-Yi
204 Mountains are in the southeast. The North China Plain is in the northeastern part of this
205 region. Three smaller plains are in the middle, namely, the Jiang-Han Plain, the
206 Dong-Ting Lake Plain and the Po-Yang Lake Plain, with the Da-Bie Mountains, the
207 Mu-Lian-Jiu Mountains and the Luo-Xiao Mountains distributed from north to south.



208

209 **Figure 1.** (a) The coverage of BT data (blue rectangle) in the present study and the
 210 boundary of the middle reaches of the YRB (red line). (b) The terrain height (m) in the
 211 middle reaches of the YRB. Mountains (MT.) and mountain areas (M.A.) are labeled in
 212 blue, and plains and lakes are labeled in red.

213 2.2 Identifying and tracking methods

214 Following Yang et al. (2020), the criteria and steps used in the present study to
 215 identify MCS are outlined as follows (Fig. 2): 1) detect CCSs with temperature ≤ -52
 216 $^{\circ}\text{C}$ and extent $\geq 5000 \text{ km}^2$ in the BT fields; 2) track CCSs at different time steps; and 3)
 217 continuous CCSs that last longer than 3 h are identified as MCSs. The first (last) time
 218 that an MCS satisfies the above criteria is considered to be MCS formation
 219 (termination). The time when the CCS of an MCS reaches its maximum extent is

221 considered to be MCS maturity.

234 The combination of areal overlap and optical flow is used in the present study to
235 track CCSs with the following steps: 1) calculate the optical flow between two
236 successive BT fields; 2) extrapolate the target CCS at the previous time by adding
237 optical flow and compare it with the CCSs at the later time, and the one with an
238 overlapping rate $\geq 30\%$ is considered the successor of the target CCS; 3) if two CCSs or
239 more satisfy the criterion of the areal overlapping rate at the later time, the one with the
240 highest overlapping rate will be considered the successor of the target CCS; 4) examine
241 the TC locations derived from the best-track dataset, and if there are any TC-related
242 clouds within the coverage of a CCS, the CCS will be excluded because the CCS is a
243 TC cloud instead of an MCS. Backward tracking is applied to find the initiation time
244 and location of an MCS. Considering that the CCS is small and develops rapidly during
245 the early stage of an MCS, no areal limitation has been applied during backward
246 tracking.

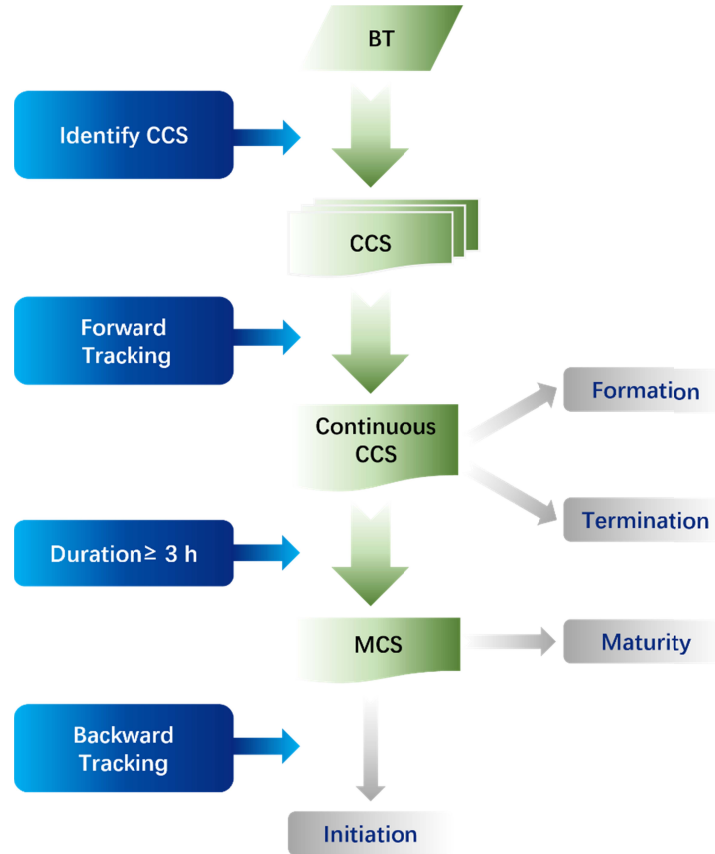


Figure 2. Flow chart of MCS identification and tracking.

236 2.3 Filtering of backward tracking

237 Backward tracking may not be accurate because the extent of a CCS is small
238 and the motion is fast during the early stage of an MCS. The splitting and regeneration
239 of MCSs, cirrus anvils, and deficiency of BT data may all lead to incorrect backward
240 tracking. Therefore, further examinations are conducted on the backward tracking
241 results. If two or more MCSs are initiated at the same time and location, it is considered
242 that those MCSs are split from the same MCS or that one MCS is regenerated from
243 another. Then, the initiation will be assigned to the earliest MCS according to the
244 formation time, and the remaining MCSs will be regarded as inaccurate tracking and
245 excluded from the MCS dataset. For the inaccurate backward tracking results caused by
246 deficiency of BT data, the filtering approach is outlined as follows: check whether the
247 BT data before the initiation time are missing; if true, the result will be regarded as
248 inaccurate and excluded from the MCS dataset. CCSs connected with cirrus anvils are
249 manually checked since they vary greatly between two successive times.

250 2.4 Objective classification

251 The *k-means* algorithm, which is widely used for classification in atmospheric
252 research due to its stable performance (Hoffmann & Schlünzen, 2013; Huth et al.,
253 2008; Kanungo et al., 2002; Ku et al., 2021; Solman & Menéndez, 2003; Stahl et al.,
254 2006; Zhang et al., 1997), is applied in the present study for the objective classification
255 of circulation patterns. The meteorological variable used for classification in the
256 present study is the geopotential height field at 700 hPa. The geopotential height field is
257 a commonly used variable in circulation classification (Hoffmann & Schlünzen, 2013;
258 Liu et al., 2019; Miao et al., 2017; Ning et al., 2020; Yang et al., 2021). Huth et al.
259 (2008) suggested that due to a high degree of dependence among individual levels, the
260 inclusion of additional levels yields little extra information over using a single level,
261 which has been confirmed in many studies (Dong et al., 2020; Liu et al., 2019; Miao et
262 al., 2017; Ning et al., 2020; Yang et al., 2021). Statistics (see Section 3) in the present
263 study suggest that MCSs are mainly initiated between 0300–0600 (Coordinated
264 Universal Time, UTC) and that 78.4% (627 out of 800) of MCSs occur in June, July
265 and August (JJA). In addition, circulation patterns vary greatly in September (Tao
266 1980). Therefore, the geopotential height fields at 700 hPa at 0000 UTC each day
267 during JJA of 2018–2021 are used for circulation classification. TCs may have a great
268 impact on synoptic circulations, leading to inaccurate classification results. Therefore,

269 based on the TC locations derived from best-track data, if a TC enters the area east of
270 124 °E and north of 20 °N on a certain day, this day will be recorded as a TC-day and
271 will be excluded during circulation classification. A total of 83 TC days are excluded.

272 The silhouette coefficient (Rousseeuw, 1987) is calculated as an approach to
273 evaluate the performance of different classification numbers. The silhouette coefficient
274 considers both the homogeneity within a class and the difference between classes (Huth
275 et al., 2008; Rousseeuw, 1987) and is widely used as criterion to determine the
276 classification number (Bernard et al., 2013; Nga et al., 2021; Ternynck et al., 2016).
277 The optimal choice of classification number in the present study is 3 based on the
278 evaluation of the silhouette coefficient.

279 2.5 Construction of proximity soundings

280 Considering the coarse temporal-spatial resolutions of the observed radiosonde
281 data, the environmental parameters in the present study are calculated from the
282 reanalysis-derived proximity soundings based on ERA5 data. However, some previous
283 studies have noted the differences in the boundary layer variables between reanalysis
284 and observed soundings and that correcting the boundary layer variables of the
285 reanalysis sounding is necessary (Gensini et al., 2014; King & Kennedy, 2019).
286 Therefore, the hourly AWS observations are used to correct surface-level variables in
287 ERA5 data before calculating environmental parameters.

288 The nearest hour before an MCS initiation and the ERA5 grid closest to the
289 initiation are chosen as the time and location, respectively, to construct a proximity
290 sounding. The closest AWS observation to the ERA5 grid within a radius of 100 km of
291 the grid is selected to correct the surface-level variables of the ERA5 data. The ERA5
292 temperature/dew-point temperature profile is first constructed based on the isobaric
293 layers (all 37 layers from 1000 hPa to 1 hPa). Then, the isobaric layers below the AWS
294 surface pressure layer are neglected, and the AWS variables are deemed the lowest
295 layer of the proximity sounding (Brooks et al., 2003; Ma et al., 2021b; Yang & Sun,
296 2018).

297 The environmental parameters are calculated based on proximity soundings to
298 investigate the dynamic and thermodynamic conditions of MCS initiation under
299 different circulation backgrounds. Ten parameters are selected, namely, the
300 surface-based convective available potential energy (SBCAPE), the most unstable

layer convective available potential energy (MUCAPE), surface-based convective inhibition (SBCIN), most unstable layer convective inhibition (SBCIN), lifted index (LI), lifted condensation level (LCL), level of free convection (LFC), precipitable water (PW), 0–3 km bulk wind shear (SHR3) and 0–6 km bulk wind shear (SHR6). These parameters, with clear physical meanings and good performances in distinguishing between different intensities and types of convection, are widely used in convection environment studies (Brotzge et al., 2013; Grams et al., 2012; J. C. Kirkpatrick et al., 2007; Ma et al., 2021b; McCaul & Weisman, 2001; Yang & Sun, 2018).

3 Statistical characteristics

3.1 MCS trajectories and paths

On the one hand, the movements and propagations of MCSs are closely related to the occurrences of convective weather phenomena; on the other hand, they represent the regulation of large-scale circulations over mesoscale systems (Li et al., 2008; Yang et al., 2020; Jiang & Fan, 2002; Mai et al., 2020). In the present study, MCSs are categorized into quasistationary (QS) and outward-moving (OM) types. For QS MCSs, both the formations and terminations occur within the study area (Fig. 1b), and OM MCSs refer to those formed within the study area but terminated outside of the study area.

During the warm seasons (April–September) of 2018–2021, 800 MCSs are identified in the middle reaches of the YRB, where 524 are QS type and 276 are OM type, accounting for 65.5% and 34.5% of the total MCSs, respectively. Based on the movement trajectories of the MCSs, those of the QS type (Fig. 3a) are short and mainly within the study area. Part (13.7%) of the QS MCSs moved outside of the study area at certain times during their life cycles; however, they moved back into and terminated within the study area. The trajectories of OM MCSs (Fig. 3b) are longer than those of QS MCSs and are mainly eastward and southward. Most of the OM MCSs terminated after propagating into the oceanic area; however, some OM MCSs with long trajectories could reach the Pacific Ocean east of Japan or north of the Indo-China Peninsula.

To further investigate the main paths of the two types of MCSs, the *k-means* algorithm is adopted to classify MCS trajectories. Based on the evaluation of the silhouette coefficient, the trajectories of QS (OM) MCSs are classified into 4 (3) main

333 paths. Among the 4 paths of the QS MCSs (Fig. 3c), the number of MCSs in the
 334 southeast path is the largest, and the northwest path is the smallest. The lengths of the
 335 northeast and southeast paths are long, while those of the northwest and southwest
 336 paths are short. For the southeast and northeast paths, the average locations of MCS
 337 initiation are both located in the western Hunan mountainous area. For the southwest
 338 path and the northwest path, the average locations are in the western slope of the
 339 Mu-Lian-Jiu Mountains and the northern edge of the Luo-Xiao Mountains,
 340 respectively. Except for the northwest path with the smallest number of MCSs, the
 341 other 3 paths all move from the mountains to the plains. The phenomenon that
 342 convections are initiated in mountainous areas and propagate to the plains often occurs
 343 in the Rocky Mountains and the Great Plains of the United States (Carbone et al., 2002;
 344 Zhang et al., 2014) and the Tai-Hang Mountains and the North China Plain (He &
 345 Zhang, 2010; Zhu et al., 2018), which is related to the mountain-plain solenoid driven
 346 by thermodynamic effects (Bao et al., 2011; Sun & Zhang, 2012; Zhang & Sun, 2017).
 347 For the OM MCSs, among the 3 paths (Fig. 3d), the number of MCSs in the southeast
 348 path is the largest. The northeast path has the longest length, followed by the southeast
 349 path, and the southwest path has the shortest length. For the northeast path, the average
 350 location of MCS initiation is east of the Yangtze-Han Plain, and for the southeast path
 351 and the southwest path, the average locations are in the Mu-Lian-Jiu Mountains and the
 352 Luo-Xiao Mountains, respectively.

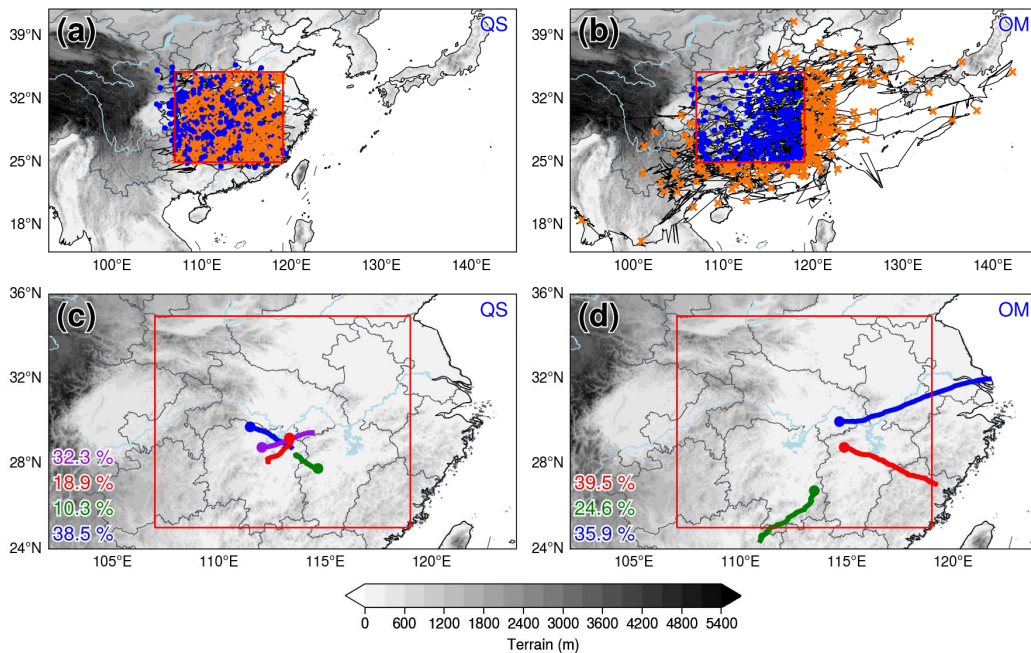
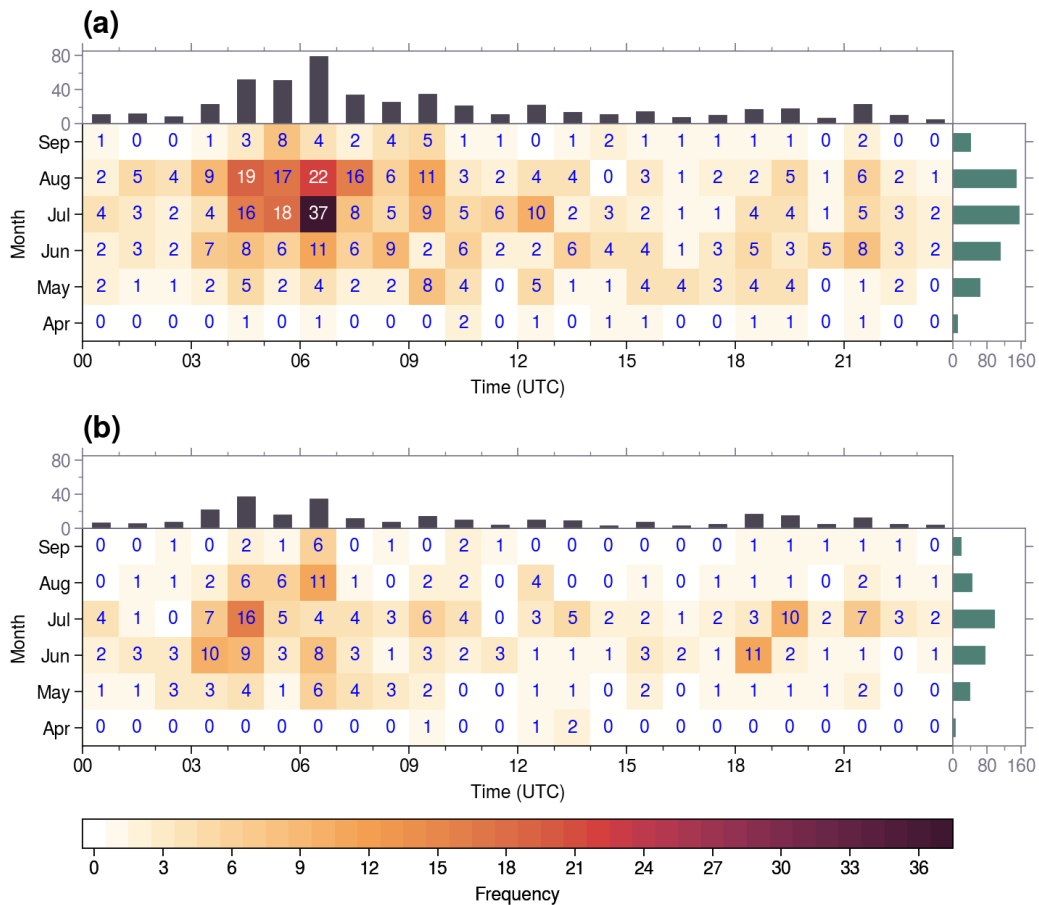


Figure 3. The movement trajectories of QS MCSs (a) and OM MCSs (b) and the composite movement paths of QS MCSs (c) and OM MCSs (d). The blue dots (orange crosses) in (a) and (b) represent the initiation (termination) locations of MCSs. Different paths are distinguished by different colors in (c) and (d), and the proportions of trajectories in different paths are marked in the lower left corner. The gray shading represents terrain height (m). The red rectangle indicates the boundary of the middle reaches of the YRB.

3.2 Temporal-spatial distribution of MCSs' initiations

The temporal distributions of MCS initiation are shown in Fig. 4. The QS MCSs mostly occur in July, followed by August (Fig. 4a), while the OM MCSs occur most frequently in July, followed by June (Fig. 4b). During the Mei-yu season in the YRB, namely, mid-June to mid-July (Tao, 1980), the mesoscale systems basically move eastward along the Mei-yu front. After mid-July, the convections in this area are mainly caused by local diabatic effects. These results explain why QS MCSs mostly occur in July and August, while OM MCSs mostly occur in June and July (Zhang et al., 2014). The QS MCSs are mainly (41.2%) initiated around noon (0400–0800 UTC), and the peak time is 0600–0700 UTC, which is identical in each month (Fig. 4a). However, the peak hours of initiation for OM MCSs vary in different months. In June and July, the initiation of OM MCSs has two peaks, one at noon (0300–0500 UTC) and the other at night (1800–1900 UTC). The noon peak is generally considered to be related to the instability caused by surface solar heating (Yu et al., 2007), and MCSs initiated during this time period correspond to the afternoon peak of summer precipitation in the YRB (Luo et al., 2016; Zhang et al., 2020). The mechanism for the late-night peak is complicated, which may result from instability due to nocturnal radiative cooling at the cloud top (Lin et al., 2000), water vapor accumulation at low levels in the evening (Kubota & Nitta, 2001), or diurnal variation in local circulation forced by complex terrain (He & Zhang, 2010; Li et al., 2005; Sun & Zhang, 2012; Zhang & Sun, 2017). Regardless of the triggering mechanism, the late-night initiation peak of the OM MCS corresponds to the morning peak of precipitation in the typical Mei-yu seasons (Luo et al., 2016; Zhang et al., 2020). In other months (except for September, which has only 4 MCSs), OM MCSs have only one peak in the afternoon (0600–0700 UTC), which is consistent with the QS type.



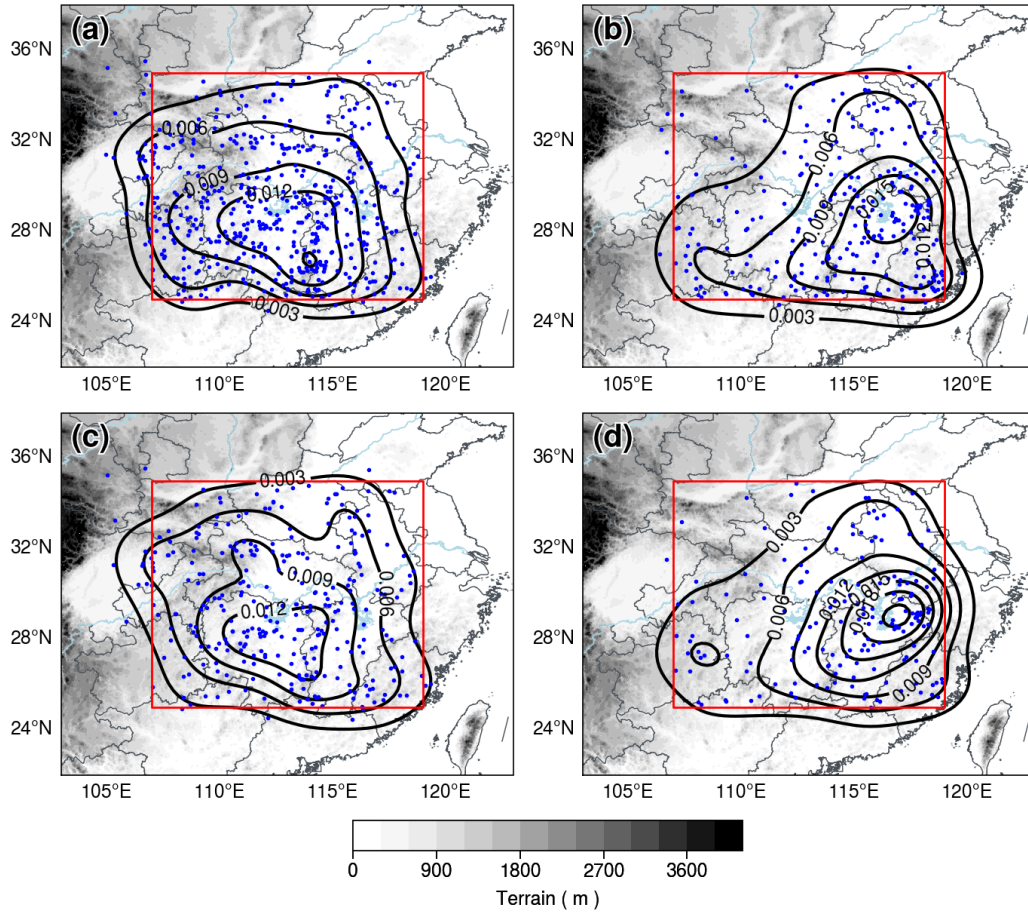
386

387 **Figure 4.** Monthly and diurnal distributions of the QS MCS frequency (a) and the OM
 388 MCS frequency (b) in the middle reaches of the YRB during the warm seasons (April–
 389 September) of 2018–2021. The horizontal axis represents the initiation time (UTC).
 390 The color shading symbolizes the occurrence frequency of MCSs.

391 The spatial distributions of MCS initiation are shown in Fig. 5. Both the QS
 392 MCSs (Fig. 5a) and the OM MCSs (Fig. 5b) are initiated mainly in the southern part of
 393 the YRB, which is consistent with a previous study (Zheng et al., 2008). Dividing the
 394 southern part of the YRB from the north roughly by 30 °N, 343 QS MCSs and 195 OM
 395 MCSs are initiated in the southern part of the YRB, accounting for 65.5% and 70.7% of
 396 their total amounts, respectively. The highest initiation frequency of QS MCSs is found
 397 over the western Hunan mountains, the Mu-Lian-Jiu Mountains and the Luo-Xiao
 398 Mountains, while that of the OM MCSs is over the Po-Yang Lake Plain. The
 399 convection in mountainous areas is mainly driven by the thermodynamic forcing
 400 (Astling, 1984; Panosetti et al., 2016; Zhu et al., 2018), while in plain areas, due to the

401 lack of dynamic forcing or diabatic heating resulting from the complex terrain, the
402 initiation of convection is mostly related to synoptic circulation systems (Reif &
403 Bluestein, 2017; Wilson & Roberts, 2006), which explains why QS MCSs are more
404 likely to be initiated over mountainous areas, while OM MCSs tend to be initiated over
405 plain areas.

406 To better illustrate the spatial distributions of MCS initiation, July and August
407 (June and July) are chosen as the high occurrence period for QS (OM) MCSs. For QS
408 MCSs, the spatial distribution of initiation in July and August (Fig. 5c) is basically the
409 same as in the entire warm season (Fig. 5a), and the highest initiation frequency is also
410 over the western Hunan mountains, the Mu-Lian-Jiu Mountains and the Luo-Xiao
411 Mountains, with the highest probability density of 0.015 (0.014 for the entire warm
412 season). This consistency further indicates that the initiation of QS MCSs in the middle
413 reaches of the YRB is mainly caused by local thermodynamic effects and varies little in
414 different months. For the OM MCSs, the spatial distribution of initiation in June and
415 July (Fig. 5d) exhibits some differences compared with that of the entire warm season
416 (Fig. 5b). Over the Po-Yang Lake Plain, the maximum probability density increases
417 from 0.017 to 0.022, indicating that in June and July, OM MCSs are more likely to be
418 initiated over the plain areas. In addition, the probability density contours extend from
419 the maximum over Po-Yang Lake to the southwest along the Luo-Xiao Mountains and
420 to the southeast along the Wu-Yi Mountains in the entire warm season, showing close
421 relationships to orographic effects, but in June and July, the probability density
422 contours show fewer extensions outward from the maximum center, indicating that the
423 initiation of OM MCSs is less related to the terrain in June and July.



424

425 **Figure 5.** The spatial distribution of initiation locations of QS MCSs during the entire
 426 warm season (a) and in July and August (c) and OM MCSs during the entire warm
 427 season (b) and in June and July (d). The blue dots represent initiation locations, from
 428 which the spatial probability density is calculated and exhibited by the black contours.
 429 The red rectangle marks the middle reaches of the YRB. The gray shading represents
 430 terrain height (m).

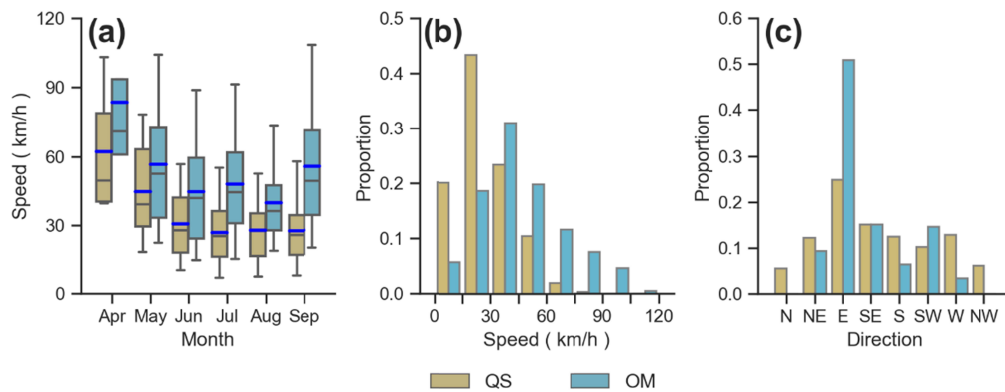
431

3.3 Features of MCSs' movement

432

The moving velocity of an MCS between two consecutive times is calculated
 433 based on the centroid locations and the time interval. The average moving velocity of
 434 all times in the entire life cycle of an MCS is considered to be the bulk moving velocity
 435 of the MCS. In general, the speeds of OM MCSs are faster than those of QS MCSs (Fig.
 436 6a). The movement of the MCS is regulated by the steering wind in the mid-lower
 437 troposphere (Rehbein et al., 2018); therefore, both the QS and OM MCSs move faster
 438 in April and May and slower in June, July and August. The speeds of the QS (OM)

452 MCSs are basically the same in July and August (June and July), indicating that the
 453 selection of a high occurrence period is reasonable. The speeds and directions of QS
 454 MCSs and OM MCSs in their high occurrence period are shown in Figs. 6 b and c.
 455 More than 80% of QS MCSs move at speeds of 0–45 km h⁻¹, and the highest proportion
 456 is located in the range of 15–30 km h⁻¹, accounting for 44% of all QS MCSs. Most
 457 (more than 70%) OM MCSs move at speeds of 15–60 km h⁻¹, with the highest
 458 proportion in the range of 30–45 km h⁻¹, accounting for 32%. The moving directions of
 459 the QS MCSs are relatively evenly distributed in all 8 directions in July and August
 460 with roughly similar proportions, which also indicates that the QS MCSs in July and
 461 August are less related to the activities of synoptic systems. The synoptic systems in the
 462 middle reaches of the YRB generally move eastward (Fu et al., 2011a; Zhang et al.,
 463 2018; Zhang & Sun, 2017), resulting in more than 50% of OM MCSs moving eastward
 464 and no OM MCS moving north or northwestward.



453
 459 **Figure 6.** Box-and-whisker plot of MCS speed (a, km h⁻¹) during the warm seasons of
 460 2018–2021 (a). The upper and lower edges (caps) of the boxes (whiskers) in the
 461 box-and-whisker plot represent the 3rd and 1st quartiles (95th and 5th percentiles),
 462 respectively. The black (blue) dashes inside boxes represent the medians (mean values).
 463 Histograms of MCS movement speeds (b, km h⁻¹) and directions (c) in the high
 464 occurrence period.

460 3.4 Duration, maximum extent and lowest temperature of MCSs

463 The duration and maximum extent represent the temporal-spatial scale of an
 464 MCS, and the lowest brightness temperature may reflect the intensity of the strongest
 465 convection in the MCS. In this section, box-and-whisker plots are applied to examine

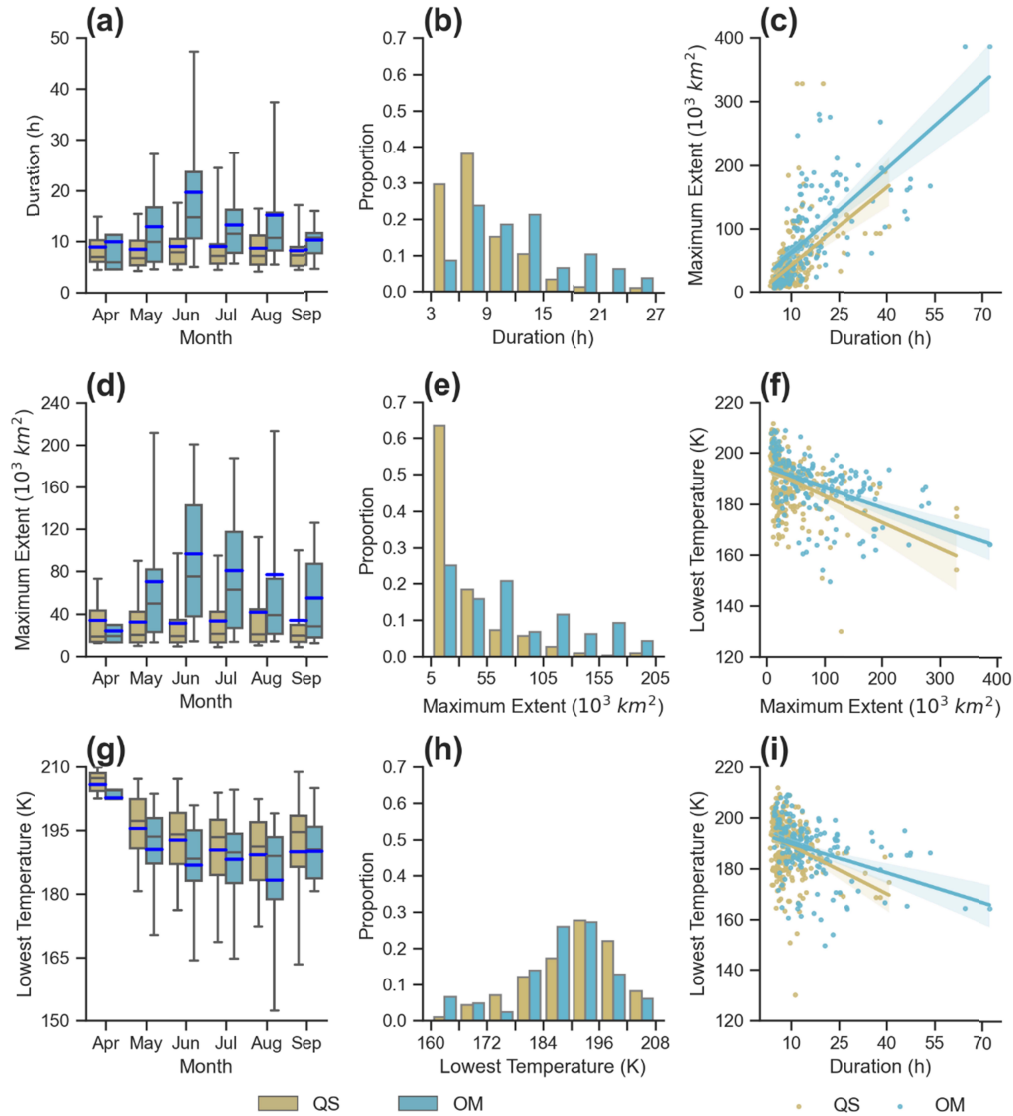
the distributions of the three features in the entire warm season (Figs. 7 a, d and g). Then, the proportion distributions (Figs. 7 b, e and h) and the pairwise relationships (Figs. 7 c, f and i) of these features in the high occurrence period (July and August for the QS MCSs and June and July for the OM MCSs) are analyzed.

Basically, the OM MCSs last longer than the QS MCSs (Fig. 7 a). The QS MCSs mainly last for 5–10 h, with no significant variations between different months. The OM MCSs in June last longer than those in other months, with an average duration of ~20 h. The maximum extents of QS MCSs are mainly smaller than $5 \times 10^4 \text{ km}^2$, while those of OM MCSs are mostly between $2 \times 10^4 \text{ km}^2$ and $1.5 \times 10^5 \text{ km}^2$ and vary from month to month. The lowest temperature shows a similar distribution between the QS MCSs and the OM MCSs with an average value of approximately 190 K. The mechanisms of initiation and development of QS MCSs are related to the local thermodynamic effects, resulting in little difference in duration and maximum extent between months. However, OM MCSs are mainly caused by synoptic systems that vary in different months in the middle reaches of the YRB (Wang et al., 2021; Sun et al., 2018), leading to complexity in the mechanisms of the initiation and development of OM MCSs, further resulting in differences in duration and maximum extent between months.

In July and August, nearly 40% of QS MCSs last 6–9 h and 30% last 3–6 h. In June and July, more than 60% of OM MCSs last 6–15 h, with ~20% of each 3-h interval. The maximum extents of QS MCSs in July and August are mainly 5×10^3 – $3 \times 10^4 \text{ km}^2$, accounting for more than 60%, while the maximum extents of the OM MCSs in June and July are distributed evenly in the 5×10^3 – $3 \times 10^4 \text{ km}^2$, 3×10^4 – $5.5 \times 10^4 \text{ km}^2$ and 5.5×10^4 – $8 \times 10^4 \text{ km}^2$ intervals, with each accounting for ~20%. For the lowest temperature, half of the QS (OM) MCSs are 184–196 K (190–202 K) in July and August (June and July).

Based on the above analysis, there are certain connections among the duration, maximum extent and lowest temperature of MCSs. The pairwise correlations of the three features in the high occurrence period are shown in Figs. 7 c, f and i. In general, the longer the durations of the MCSs are, the larger the maximum extents and the colder the cloud tops. With the extension of duration, the maximum extent shows an enlarging trend (Fig. 7c), which is consistent between the QS type and the OM type. With the increase in the maximum extent, the lowest temperature decreases (Fig. 7f), and that of

the QS type decreases faster than that of the OM type. With increasing duration, the lowest temperature shows a decreasing trend (Fig. 7i), and that of the QS MCSs also decreases faster.



500

Figure 7. The box-and-whisker plots on the left are the duration (a), the maximum extent (d) and the lowest temperature (g) of MCSs during the entire warm seasons of 2018–2021. The upper and lower edges (caps) of the boxes (whiskers) in the box-and-whisker plot represent the 3rd and 1st quartiles (95th and 5th percentiles), respectively. The black (blue) dashes inside boxes represent the medians (mean values). The histograms of the central column are the proportion of the duration (b), the maximum extent (e) and the lowest temperature (h) of MCSs in high occurrence

507 periods of 2018–2021. The scatter plots on the right are the pairwise relationships
508 between the duration and the maximum extent (c), the maximum extent and the lowest
509 temperature (f), and the duration and the lowest temperature (i) in high occurrence
510 periods of 2018–2021.

511 3.5 Diurnal variation in maximum extent and lowest temperature

512 To investigate the diurnal variation in the MCSs in the middle reaches of the
513 YRB, the time when the maximum extent (lowest temperature) appears and the time
514 span between MCS initiation and the maximum extent (lowest temperature) appearance
515 are further examined. Since 58% of QS MCSs are initiated in July and August and 62%
516 of OM MCSs occur in June and July, to highlight the difference between QS MCSs and
517 OM MCSs, only MCSs in high occurrence periods are analyzed, and the results are
518 shown in Fig. 8.

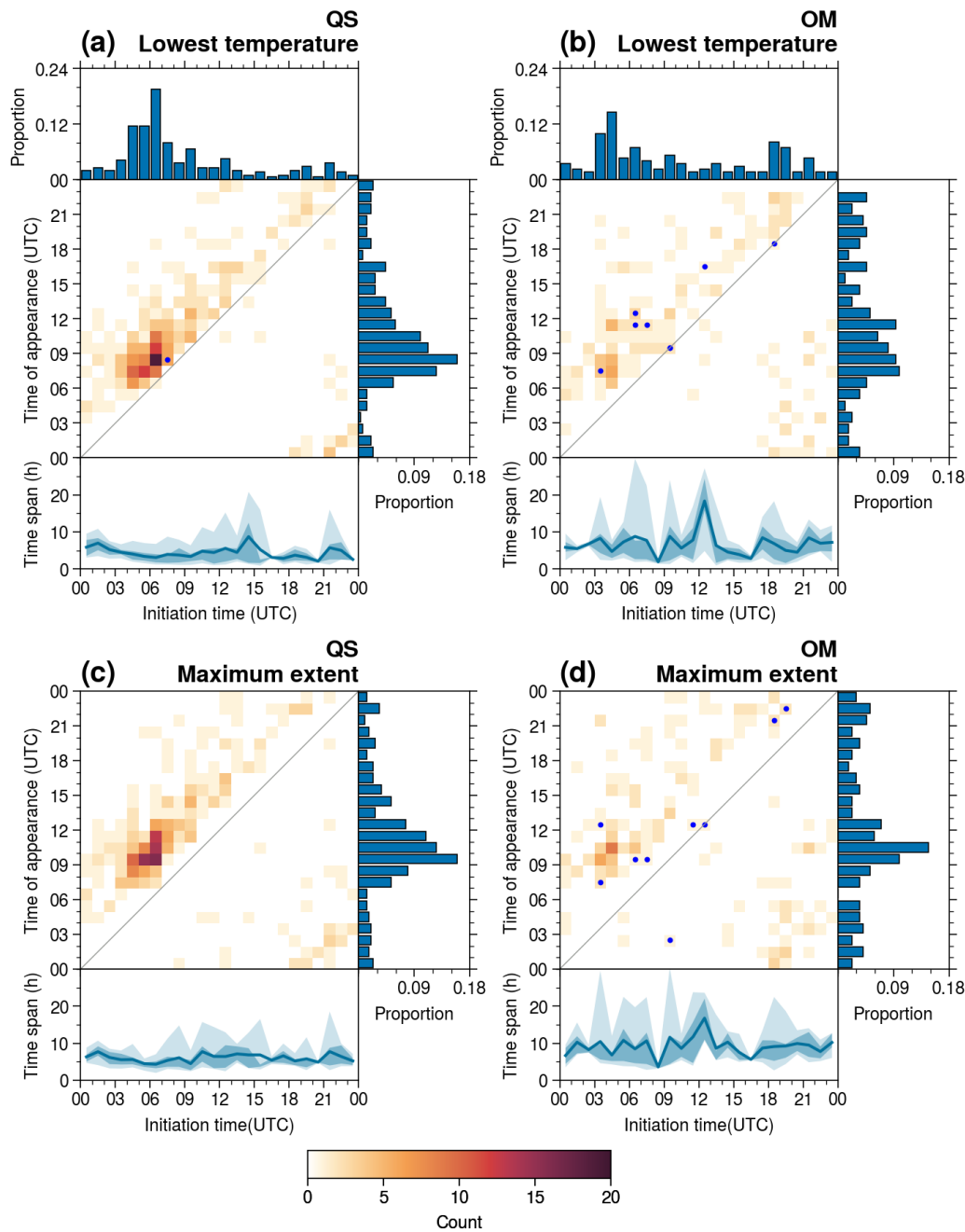
519 In July and August, the initiation frequency of QS MCSs peaks in the afternoon
520 (0600–0700 UTC, Fig. 8a, upper subplot), which is the same as the result from the
521 entire warm season (Fig. 3a). In June and July, the initiation frequency of OM MCSs
522 has two peaks, namely, noon peak (0300–0500 UTC) and late-night peak (1800–2000
523 UTC, Fig. 8b, upper subplot). For the OM MCSs, compared with the result from the
524 entire warm season (Fig. 3b), the proportions of MCS initiation during the noon peak
525 (0300–0500 UTC) and the late-night peak (1800–2000 UTC) increase, but that during
526 the afternoon peak (0600–0700 UTC) decreases.

527 In July and August, the lowest temperatures of QS MCSs mainly appear in the
528 afternoon (0700–1100 UTC), with a peak at 0800–0900 UTC (Fig. 8a, the main plot
529 and the subplot on the right-hand side). The surface solar heating is the strongest in the
530 afternoon; therefore, convective activities are most vigorous during this time period. In
531 June and July, the lowest temperatures of OM MCSs mainly appear in the afternoon
532 and the evening, distributed evenly during this time period without any obvious peak
533 (Fig. 8b, the main plot and the subplot on the right-hand side). As mentioned before,
534 OM MCSs are mainly associated with synoptic circulation systems, and the
535 mechanisms for convection development are complicated, resulting in no obvious peak
536 for the lowest temperature appearance. In July and August, the maximum extents of QS
537 MCSs mainly appear in the evening (0900–1200 UTC, Fig. 8c, the main plot and the
538 subplot on the right-hand side), 1–2 h later than the appearance of the lowest

539 temperature. In June and July, the maximum extents of OM MCSs mainly appear in the
540 evening (0900–1100 UTC) (Fig. 8d, the main plot and the subplot on the right-hand
541 side).

542 In July and August, the lowest temperatures (the maximum extents) of the QS
543 MCSs appear 4.43 h (6.03 h) after initiation. The QS MCSs initiated at noon or in the
544 afternoon (0500–1000 UTC) reach the lowest temperature ~3 h after initiation (Fig. 8a,
545 lower subplot), which indicates that the QS MCSs caused by local thermodynamic
546 effects in this time period develop at roughly the same pace. The QS MCSs in July and
547 August mainly achieve the maximum extent 4–7 h after initiation (Fig. 8c, lower
548 subplot). In June and July, the lowest temperatures (maximum extents) of the OM
549 MCSs appear 6.8 h (9.21 h) after initiation (lower subplots in Figs. 8 b and d). The
550 development of OM MCSs is associated with many factors (i.e., synoptic systems,
551 orography, and underlying surface) and interactions between these factors; therefore,
552 the diurnal variations follow no obvious pattern.

553



554

555 **Figure 8.** The two-dimensional histogram for the diurnal variation in the lowest
 556 temperature appearance of QS MCSs (a) and OM MCSs (b) and the maximum extent
 557 appearance of QS MCSs (c) and OM MCSs (d) in the high occurrence period of 2018–
 558 2021. The main body of each plot exhibits the frequency of MCS initiation and the
 559 lowest temperature (maximum extent) in every hourly interval. The upper histogram
 560 exhibits the proportion of MCS initiation. The left histogram exhibits the proportion of
 561 the lowest temperature (maximum extent) appearance. The lower plot exhibits the time

span between the lowest temperature (maximum extent) appearance and MCS initiation, with the solid line representing the mean time span and the light (dark) shading representing the 5%–95% (25%–75%) percentile interval. The blue dot indicates that the time span is longer than 24 h.

4 Circulation patterns and environmental conditions for MCS initiation

To investigate the circulation patterns favorable for MCS initiation, the daily circulations at 0000 UTC in JJA of 2018–2021 are objectively classified into 3 patterns by adopting the *k-means* algorithm, and the environmental parameters under different circulation patterns are further analyzed.

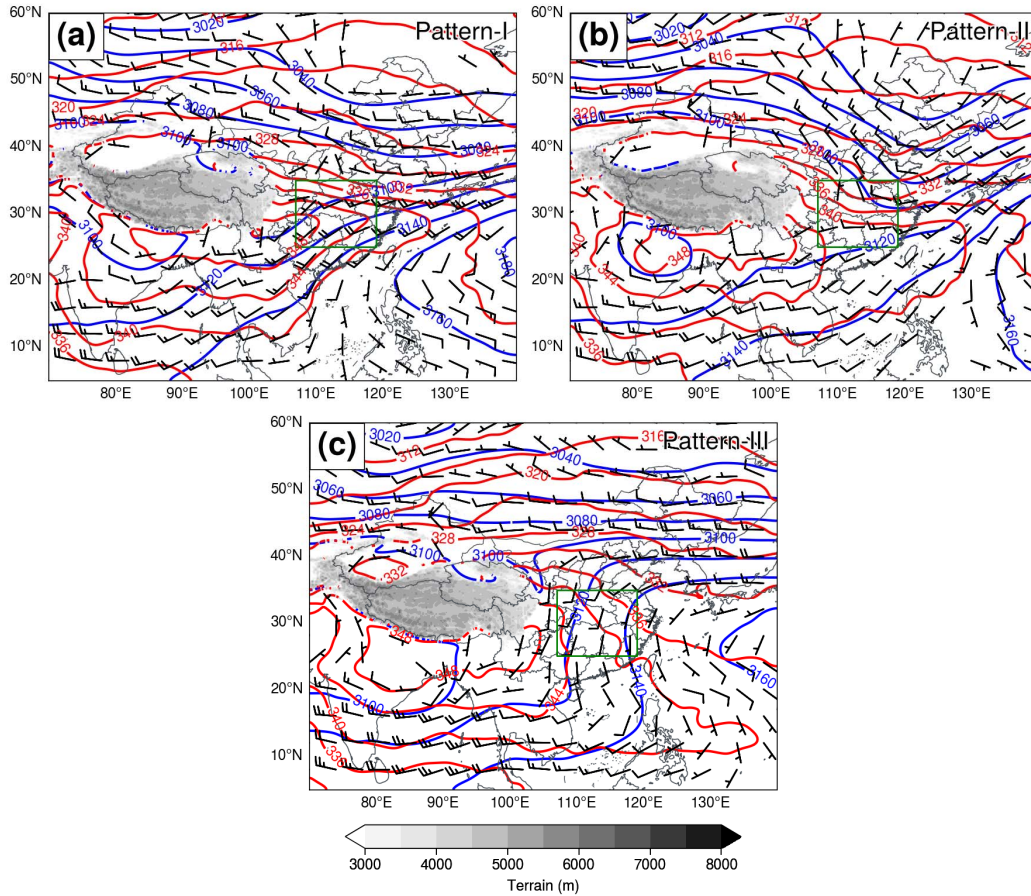
4.1 Objective classification of circulation patterns

Circulations of 285 days without direct influencings from tropical cyclones in JJA of 2018–2021 are classified into 3 patterns according to the evaluation based on the silhouette coefficient, with 128, 66 and 91 days in each pattern, respectively, and the composite fields of geopotential height at 700 hPa are shown in Fig. 9. Pattern-I (P1) is the typical circulation of the Mei-yu front (Fig. 9a). With a shallow trough in northeast China and the Indo-China Peninsula, the middle reaches of the YRB are in a large-scale convergence zone formed by the northwesterlies from the high latitudes and the southwesterlies from the low latitudes, which is consistent with the shear line and the strong equivalent potential temperature gradient. In Pattern-II (P2), the middle reaches of the YRB are basically under the control of the northwesterly, to the east of which is a deep trough (Fig. 9b). Although the equivalent potential temperature field also shows a strong gradient in P2, the thermodynamic characteristics of circulations in P1 and P2 are different. In P1, a warm humid air flow is dominated by the strong southwesterly, with a warm tongue extending from southwest to northeast. In P2, the northwesterly is the dominant wind, steering a cold tongue extending from north to south. The equivalent potential temperature field in P1 (336–348 K) is higher than that in P2 (332–340 K), indicating that the air mass in P1 is warmer or wetter than that in P2. In Pattern-III (P3), the middle reaches of the YRB are under the control of the weak southerly to the east of the Western Pacific Subtropical High.

A total of 330 QS MCSs and 187 OM MCSs are initiated during JJA of 2018–2021. Fifty percent of QS MCSs and 59.9% of OM MCSs are initiated in P1, suggesting that P1 is favorable for both QS and OM MCS initiation. Thirteen percent (36.1%) of

the QS MCSs and 25.7% (14.4%) of the OM MCSs are initiated in P2 (P3). The daily average initiation frequencies of QS MCSs in the three patterns are 1.31, 0.65 and 1.31, and those of the OM MCSs are 0.88, 0.72 and 0.3, respectively. In general, the QS MCS initiation in P1 and P3 is the same and in P2 is the least, while the OM MCSs are initiated the most in P1, followed by P2 and the least in P3.

599



600

Figure 9. The composite geopotential fields (blue contours, gpm), equivalent potential temperature fields (red contours, K) and wind fields (wind barbs, m s^{-1}) at 700 hPa of Pattern-I (a), Pattern-II (b) and Pattern-III (c), respectively. A half (full) barb represents 2 m s^{-1} (4 m s^{-1}). The green rectangle marks the middle reaches of the YRB. The gray shading represents terrain heights (m).

606

4.2. Environmental parameters

607

608 To investigate the dynamic and thermodynamic conditions for MCS initiation under the three circulation patterns, ten environmental parameters are statistically

609 analyzed, and the results are shown in Fig. 10.

610 The mean value of SBCAPE in P1 (Fig. 10 a) is 2363 J kg^{-1} and that of
611 MUCAPE is 2491 J kg^{-1} , both the lowest in the three patterns. A low CAPE often
612 implies a high LFC height or a small environmental lapse rate, yet the LFC height in P1
613 is the lowest in the three patterns (Fig. 10g) with a mean value of 743 m, which suggests
614 that the lapse rate of the mid-low troposphere in P1 is small. The mean value of LI in P1
615 (Fig. 10e) is -4.4 K , the highest in the three patterns, which also confirms this
616 conclusion. The mean PW in P1 (Fig. 10h) is 65 mm, which is significantly higher than
617 those in P2 and P3. The contribution to the local water vapor growth in the YRB often
618 came from the southwesterly and southeasterly originating from the oceans (Li et al.,
619 2014; Shi et al., 2020; Wang et al., 2021), which is consistent with the synoptic
620 circulation in P1.

621 The mean SHR3 (Fig. 10i) and SHR6 (Fig. 10j) in P1 are 9 m s^{-1} and 8.9 m s^{-1} ,
622 respectively, which are both significantly higher than those in P2 and P3. In P2 and P3,
623 the SHR6s are basically 1 m s^{-1} higher than the SHR3s (both the median and mean
624 value). However, in P1, the medians of SHR6 and SHR3 are basically equal, and the
625 mean values of SHR6 are even lower than those of SHR3. There is little difference
626 between SHR3 and SHR6 in P1, but the SHR6s in P2 and P3 are higher than the
627 SHR3s, which suggests that the wind speed in the low troposphere in P1 is high or that
628 MCS initiation in P1 may often be accompanied by low-level jets. Higher vertical wind
629 shears in P1 may be the reason why OM MCSs tend to occur in P1 (Cohen et al., 2007).

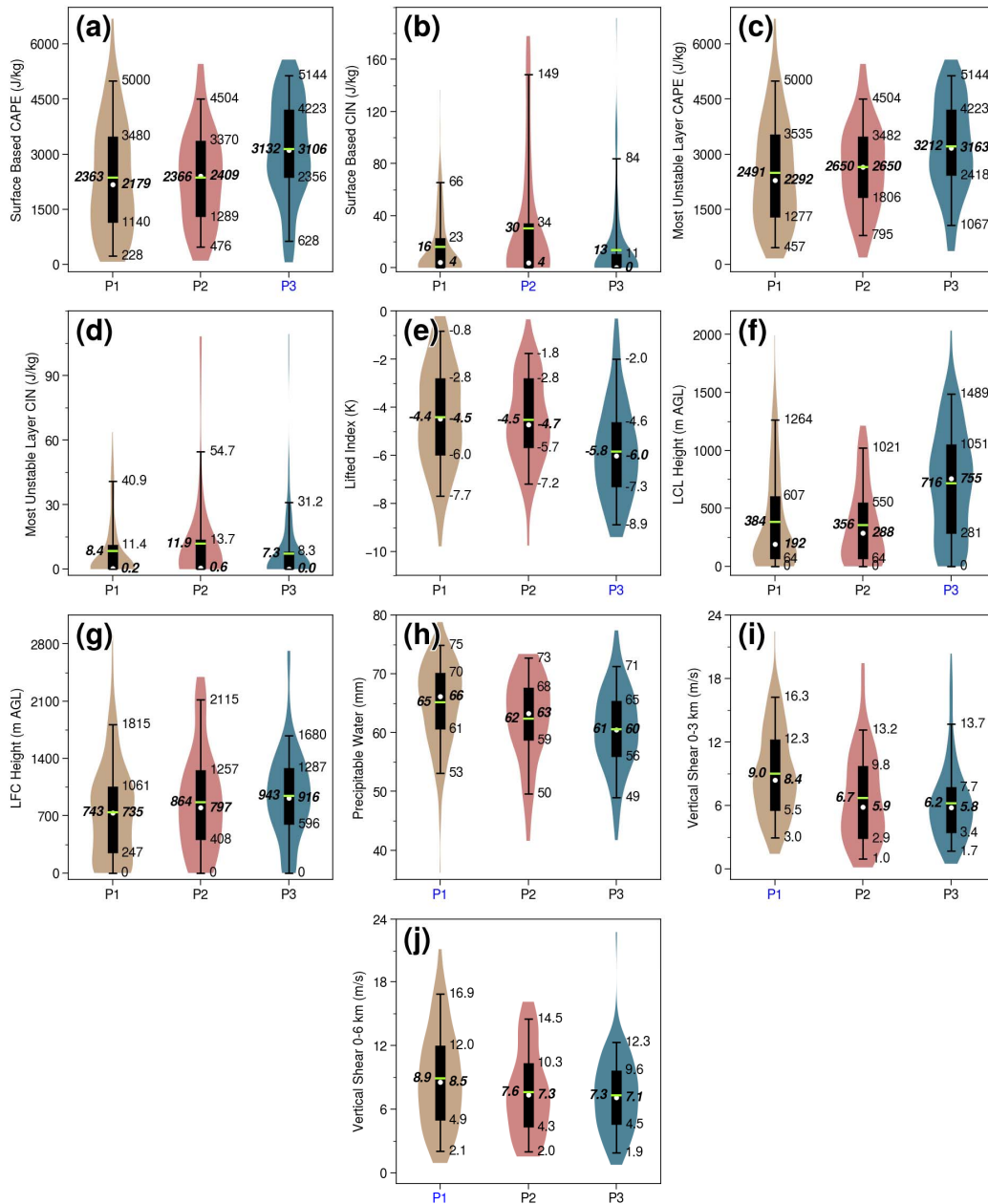
630 The mean SBCAPE (MUCAPE) in P2 is 2366 J kg^{-1} (2650 J kg^{-1}). The
631 difference between MUCAPE and SBCAPE in P2 is the largest among the three
632 patterns, indicating that the atmosphere in the boundary layer in P2 is more stable than
633 those in P1 and P3, which is consistent with the composite circulation in P2, dominated
634 by northerlies. In operational forecasts, a stable boundary layer and a low CAPE can be
635 misleading and cause the possible elevated convections to be ignored. The mean
636 SBCIN in P2 is 30 J kg^{-1} (Fig. 10b), and the mean MUCIN in P2 is 11.9 J kg^{-1} (Fig.
637 10d), and both SBCIN and MUCIN were significantly higher than those in P1 and P3.
638 In P2, 25% of MCSs are initiated in the environment with SBCIN greater than 34 J kg^{-1}
639 (Fig. 10b). The large SBCIN in P2 confirms the aforementioned conclusion that the
640 low-level atmosphere in P2 is more stable than those in P1 and P3. The mean LCL
641 height in P2 (Fig. 10f) is 356 m, which is the lowest among the three patterns, and the

642 mean LFC height (Fig. 10g) is 864 m. The lowest LCL height in P2 indicates a high
643 relative humidity at the surface, which may be caused by the cold invasion related to the
644 northerly.

645 Both the mean SBCAPE (Fig. 10a) and the mean MUCAPE (Fig. 10c) in P3 are
646 3132 J kg^{-1} and are significantly higher than those in P1 and P2. More than 25% of
647 MCSs are initiated in the environment with SBCAPE over 4000 J kg^{-1} . The mean PW
648 in P3 (Fig. 10h) is 61 mm, the mean SHR3 (Fig. 10i) is 6.2 m s^{-1} , and the mean SHR6
649 (Fig. 10j) is 7.3 m s^{-1} . Although different environmental parameters are not simply
650 compensated for each other (Kirkpatrick et al., 2007), considering the lack of synoptic
651 forcing and the lowest PW (Fig. 10j) in P3, a higher CAPE may be required during
652 MCS initiation (Kirkpatrick et al., 2009; McCaul & Weisman, 2001), and it is
653 suggested that in an environment with a large CAPE, a higher LFC height and a lower
654 PW are beneficial for updrafts (Kirkpatrick et al., 2011), which is similar to the
655 configuration in P3. The mean LCL height (Fig. 10f) is 716 m and is significantly
656 higher than those in P1 and P2. The highest LCL height in P3 suggests a relatively dry
657 boundary layer (Rasmussen & Blanchard, 1998), causing stronger evaporation and
658 colder outflow from the downdrafts (Kuchera & Parker, 2006) and further resulting in
659 severe wind on the surface ground (Evans & Doswell, 2001; Kaltenböck et al., 2009).
660 The difference between the mean LFC height and the mean LCL height is smallest in
661 P3. A high LCL height suggests a dry low-level environment, and a low LFC height
662 represents a large lapse rate, which indicates that the impact of the southerly in P3 is
663 greater on warming than on humidification. This conclusion can also be confirmed by
664 the lowest PW (Fig. 10h) in P3. The mean SBCIN (Fig. 10b) is 13 J kg^{-1} and the mean
665 MUCIN (Fig. 10d) is 7.3 J kg^{-1} , and both are the minimum in the 3 patterns. Note that
666 the medians of the SBCIN and the MUCIN in P3 are both 0 J kg^{-1} , which suggests that
667 more than half of the MCSs in P3 are triggered in the environment with no CIN.
668 However, the mean LFC height in P3 is the highest, combined with the minimum CIN,
669 representing a dry-adiabatic or even superadiabatic low-level atmosphere, which
670 confirms the conclusion that the southerly in P3 is more favorable for warming than for
671 humidifying.

672

673



674

675 **Figure 10.** Violin plots of environmental parameters. From (a) to (j) are SBCAPE (J
676 kg^{-1}), SBCIN (J kg^{-1}), MUCAPE (J kg^{-1}), MUCIN (J kg^{-1}), LI (K), LCL (m), LFC (m),
677 PW (mm), SHR3 (m s^{-1}), and SHR6 (m s^{-1}). The outline of the violin represents the
678 probability density. The upper and lower edges (caps) of the box (whiskers) inside the
679 violin represent the 3rd and 1st quartiles (95th and 5th percentiles), respectively, which
680 are marked on the right side of the violin. The white dot (lemon dash) inside the box
681 represents the median (mean value), which is marked in bold italics on the right (left).
682 The pattern label marked blue indicates that the mean value of the parameter in this

683 pattern is significantly (above the 95% level based on a two-tailed Welch's t test)
684 different from those in the other two patterns.

685 **5 Summary and conclusions**

686 Based on the BT data from the Advanced Geosynchronous Radiation Imager
687 onboard the FY-4A satellite during the warm seasons (April–September) of 2018–
688 2021, the combination of areal overlapping and optical flow is adopted to identify and
689 track the MCSs in the middle reaches of the YRB, which are categorized into the
690 quasistationary (QS) type and the outward-moving (OM) type and are statistically
691 analyzed. The daily circulations of JJA, during which MCSs occur most frequently, are
692 objectively classified into three patterns using the *k-means* algorithm, and the
693 environmental conditions of MCS initiation are further compared and analyzed. The
694 main conclusions are described as follows:

695 (1) During the warm seasons of 2018–2021, 524 QS MCSs and 276 OM MCSs
696 are identified in the middle reaches of the YRB. Among the four main moving paths
697 (i.e., northeast path, southeast path, northwest path and southwest path) of QS MCSs,
698 the occurrence frequency in the southeast path is the highest. The QS MCSs are mostly
699 initiated over mountainous areas and then propagate to the plains. The moving
700 trajectories of OM MCSs are classified into three paths, namely, the northeast path, the
701 southeast path and the southwest path, among which the southeast path has the largest
702 amount of OM MCSs.

703 (2) The QS MCSs primarily occur in July and August and are mainly initiated in
704 the afternoon (0600–0700 UTC). The OM MCSs mostly occur in June and July with
705 two initiation peaks at noon (0300–0500 UTC) and late night (1800–1900 UTC),
706 respectively, corresponding to the afternoon peak and morning peak of the typical
707 precipitation associated with Mei-yu fronts. QS MCSs are mainly initiated in
708 mountainous areas and caused by local thermal effects, while OM MCSs are mostly
709 triggered in plain areas, which is related to synoptic circulation forcings.

710 (3) The OM MCSs move faster than the QS MCSs and mostly propagate
711 eastward. The durations and maximum extents of QS MCSs show no obvious
712 differences among different months, while those of OM MCSs vary among different
713 months. The lowest brightness temperatures of QS MCSs mostly appear in the
714 afternoon (0800–0900 UTC), but those of the OM MCSs exhibit no obvious diurnal

715 variation.

716 (4) Circulations at 0000 UTC of 285 MCS days, without direct influencings
717 from tropical cyclones, are classified into 3 patterns using the k-means algorithm. The
718 composite circulation of P1 is consistent with the typical circulation of the Mei-yu
719 front, and those of P2 and P3 are dominated by the northwesterly and the weak
720 southerly, respectively. The mean initiation frequencies of the QS MCSs in P1 and P3
721 are the same and that in P2 is the lowest. The OM MCSs are initiated the most in P1,
722 followed by P2, and they are initiated the least in P3.

723 (5) Analysis of the environmental conditions favorable for MCS initiation in the
724 three circulation patterns suggests that a) the low-level wind speed in P1 is relatively
725 high, and the MCS initiations in P1 may be accompanied by low-level jets, which is
726 more favorable for OM MCS initiation and propagation; b) the circulation in P2 is
727 dominated by northwesterlies with a relatively stable layer in the low-level
728 troposphere; and c) the southerly in P3 accompanied by adiabatic warming establishes
729 a dry-adiabatic or even a superadiabatic layer and further lowers the stability.

730 In the present work, a comprehensive analysis was conducted on the MCSs in
731 the middle reaches of the YRB during the warm seasons of 2018–2021, focusing
732 mainly on the statistical characteristics, circulation patterns, and environmental
733 conditions favorable for MCS initiation, and some conclusions with scientific
734 significance and utility value were obtained. However, some problems remain
735 unsolved. For example, the late-night triggering peak of OM MCSs is not well
736 understood, and the impacts of orography on MCSs in the middle reaches of the YRB
737 need further exploration. Further work will focus on these issues.

738 **Acknowledgments**

739 This research was supported by the National Natural Science Foundation of
740 China (Grant U2142202, 41975056 and 41975057).

741 **Data Availability Statement**

742 The FY-4A BT data can be downloaded from <http://data.cma.cn/> with approval
743 of China Meteorological Administration. The ERA5 dataset can be downloaded freely
744 from <https://cds.climate.copernicus.eu/cdsapp#!/home>. The TC best-track dataset can
745 be downloaded freely from https://tcdata.typhoon.org.cn/zjljsjj_zlhq.html.

746 **References**

- 747 Astling, E. G. (1984). On the relationship between diurnal mesoscale circulations and
748 precipitation in a mountain valley. *Journal of Applied Meteorology and*
749 *Climatology*, 23(12), 1635–1644.
750 [https://doi.org/10.1175/1520-0450\(1984\)023<1635:OTRBDM>2.0.CO;2](https://doi.org/10.1175/1520-0450(1984)023<1635:OTRBDM>2.0.CO;2)
- 751 Augustine, J. A., & Howard, K. W. (1988). Mesoscale convective complexes over the
752 United States during 1985. *Monthly Weather Review*, 116(3), 685–701.
753 [https://doi.org/10.1175/1520-0493\(1988\)116<0685:MCCOTU>2.0.CO;2](https://doi.org/10.1175/1520-0493(1988)116<0685:MCCOTU>2.0.CO;2)
- 754 Bai, L., Chen, G., & Huang, L. (2020). Convection initiation in monsoon coastal areas
755 (South China). *Geophysical Research Letters*, 47(11), e2020GL087035.
756 <https://doi.org/10.1029/2020GL087035>
- 757 Bao, X., Zhang, F., & Sun, J. (2011). Diurnal variations of warm-season precipitation
758 east of the Tibetan Plateau over China. *Monthly Weather Review*, 139(9), 2790–
759 2810. <https://doi.org/10.1175/MWR-D-11-00006.1>
- 760 Bechini, R., & Chandrasekar, V. (2017). An enhanced optical flow technique for radar
761 nowcasting of precipitation and winds. *Journal of Atmospheric and Oceanic*
762 *Technology*, 34(12), 2637–2658. <https://doi.org/10.1175/JTECH-D-17-0110.1>
- 763 Bernard, E., Naveau, P., Vrac, M., & Mestre, O. (2013). Clustering of maxima: spatial
764 dependencies among heavy rainfall in France. *Journal of Climate*, 26(20), 7929–
765 7937. <https://doi.org/10.1175/JCLI-D-12-00836.1>
- 766 Bister, M. (2001). Effect of peripheral convection on tropical cyclone formation.
767 *Journal of the Atmospheric Sciences*, 58(22), 3463–3476.
768 [https://doi.org/10.1175/1520-0469\(2001\)058<3463:EOPCOT>2.0.CO;2](https://doi.org/10.1175/1520-0469(2001)058<3463:EOPCOT>2.0.CO;2)
- 769 Bowler, N. E. H., Pierce, C. E., & Seed, A. (2004). Development of a precipitation
770 nowcasting algorithm based upon optical flow techniques. *Journal of Hydrology*,
771 288(1–2), 74–91. <https://doi.org/10.1016/j.jhydrol.2003.11.011>
- 772 Brooks, H. E., Lee, J. W., & Craven, J. P. (2003). The spatial distribution of severe
773 thunderstorm and tornado environments from global reanalysis data. *Atmospheric*

774 *Research*, 67–68, 73–94. [https://doi.org/10.1016/S0169-8095\(03\)00045-0](https://doi.org/10.1016/S0169-8095(03)00045-0)

775 Brotzge, J. A., Nelson, S. E., Thompson, R. L., & Smith, B. T. (2013). Tornado
776 probability of detection and lead time as a function of convective mode and
777 environmental parameters. *Weather and Forecasting*, 28(5), 1261–1276.
778 <https://doi.org/10.1175/WAF-D-12-00119.1>

779 Burton, R. R., Blyth, A. M., Cui, Z., Groves, J., Lamptey, B. L., Fletcher, J. K.,
780 Marsham, J.H., Parker, D.J. & Roberts, A. (2022). Satellite-based nowcasting of
781 west African mesoscale storms has skill at up to 4-h lead time. *Weather and*
782 *Forecasting*, 37(4), 445–455. <https://doi.org/10.1175/WAF-D-21-0051.1>

783 Carbone, R. E., Tuttle, J. D., Ahijevych, D. A., & Trier, S. B. (2002). Inferences of
784 predictability associated with warm season precipitation episodes. *Journal of the*
785 *Atmospheric Sciences*, 59(13), 2033–2056.
786 [https://doi.org/10.1175/1520-0469\(2002\)059<2033:IOPAWW>2.0.CO;2](https://doi.org/10.1175/1520-0469(2002)059<2033:IOPAWW>2.0.CO;2)

787 Cohen, A. E., Coniglio, M. C., Corfidi, S. F., & Corfidi, S. J. (2007). Discrimination of
788 mesoscale convective system environments using sounding observations. *Weather*
789 *and Forecasting*, 22(5), 1045–1062. <https://doi.org/10.1175/WAF1040.1>

790 Dong, Y., Li, J., Guo, J., Jiang, Z., Chu, Y., Chang, L., Yang, Y. & Liao, H. (2020). The
791 impact of synoptic patterns on summertime ozone pollution in the North China
792 Plain. *Science of The Total Environment*, 735, 139559.
793 <https://doi.org/10.1016/j.scitotenv.2020.139559>

794 Evans, J. S., & Doswell, C. A. (2001). Examination of derecho environments using
795 proximity soundings. *Weather and Forecasting*, 16(3), 329–342.
796 [https://doi.org/10.1175/1520-0434\(2001\)016<0329:EODEUP>2.0.CO;2](https://doi.org/10.1175/1520-0434(2001)016<0329:EODEUP>2.0.CO;2)

797 Feng, Z., Leung, L. R., Houze, R. A., Hagos, S., Hardin, J., Yang, Q., Han, B. & Fan, J.
798 (2018). Structure and evolution of mesoscale convective systems: sensitivity to
799 cloud microphysics in convection-permitting simulations over the United States.
800 *Journal of Advances in Modeling Earth Systems*, 10(7), 1470–1494.
801 <https://doi.org/10.1029/2018MS001305>

802 Feng, Z., Houze, R. A., Leung, L. R., Song, F., Hardin, J. C., Wang, J., Gustafson, W. I.

- 803 & Homeyer, C. R. (2019). Spatiotemporal characteristics and large-scale
804 environments of mesoscale convective systems east of the Rocky Mountains.
805 *Journal of Climate*, 32(21), 7303–7328. <https://doi.org/10.1175/JCLI-D-19-0137.1>
- 806 Fu, S., Sun, J., Zhao, S., & Li, W. (2011a). The energy budget of a southwest vortex
807 with heavy rainfall over south China. *Advances in Atmospheric Sciences*, 28(3),
808 709–724. <https://doi.org/10.1007/s00376-010-0026-z>
- 809 Fu, S., Sun, J., Zhao, S., Li, W. & Li, B. (2011b). A study of the impacts of the eastward
810 propagation of convective cloud systems over the Tibetan Plateau on the rainfall of
811 the Yangtze-Huai River basin. *Acta Meteorologica Sinica*, 69(4), 581–600,
812 <http://doi.org/10.11676/qxxb2011.051>. (in Chinese)
- 813 Gallus, W. A., Snook, N. A., & Johnson, E. V. (2008). Spring and summer severe
814 weather reports over the Midwest as a function of convective mode: a preliminary
815 study. *Weather and Forecasting*, 23(1), 101–113.
816 <https://doi.org/10.1175/2007WAF2006120.1>
- 817 Gensini, V. A., Mote, T. L., & Brooks, H. E. (2014). Severe-thunderstorm reanalysis
818 environments and collocated radiosonde observations. *Journal of Applied*
819 *Meteorology and Climatology*, 53(3), 742–751.
820 <https://doi.org/10.1175/JAMC-D-13-0263.1>
- 821 Grams, J. S., Thompson, R. L., Snively, D. V., Prentice, J. A., Hodges, G. M., &
822 Reames, L. J. (2012). A climatology and comparison of parameters for significant
823 tornado events in the United States. *Weather and Forecasting*, 27(1), 106–123.
824 <https://doi.org/10.1175/WAF-D-11-00008.1>
- 825 He, H., & Zhang, F. (2010). Diurnal variations of warm-season precipitation over
826 northern China. *Monthly Weather Review*, 138(4), 1017–1025.
827 <https://doi.org/10.1175/2010MWR3356.1>
- 828 He, Z., Zhang, Q., Bai, L., & Meng, Z. (2017). Characteristics of mesoscale convective
829 systems in central East China and their reliance on atmospheric circulation patterns.
830 *International Journal of Climatology*, 37(7), 3276–3290.
831 <https://doi.org/10.1002/joc.4917>

- 832 Hendricks, E. A., & Montgomery, M. T. (2006). Rapid scan views of convectively
833 generated mesovortices in sheared tropical cyclone Gustav (2002). *Weather and*
834 *Forecasting*, 21(6), 1041–1050. <https://doi.org/10.1175/WAF950.1>
- 835 Hersbach, H., Bell, B., Berrisford, P., Hirahara, S., Horányi, A., Muñoz-Sabater, J., et al.
836 (2020). The ERA5 global reanalysis. *Quarterly Journal of the Royal*
837 *Meteorological Society*, 146(730), 1999–2049. <https://doi.org/10.1002/qj.3803>
- 838 Hoffmann, P., & Schlünzen, K. H. (2013). Weather pattern classification to represent
839 the urban heat island in present and future climate. *Journal of Applied Meteorology*
840 *and Climatology*, 52(12), 2699–2714. <https://doi.org/10.1175/JAMC-D-12-065.1>
- 841 Houze, R. A. (2004). Mesoscale convective systems. *Reviews of Geophysics*, 42(4).
842 <https://doi.org/10.1029/2004RG000150>
- 843 Huth, R., Beck, C., Philipp, A., Demuzere, M., Ustrnul, Z., Cahynová, M., et al. (2008).
844 Classifications of atmospheric circulation patterns. *Annals of the New York*
845 *Academy of Sciences*, 1146(1), 105–152. <https://doi.org/10.1196/annals.1446.019>
- 846 Jiang, J. & Fan, M. (2022). Convective clouds and mesoscale convective systems over
847 the Tibetan Plateau in summer. *Chinese Journal of Atmospheric Sciences*, 26(2),
848 263–270, <http://doi.org/10.3878/j.issn.1006-9895.2002.02.12>. (in Chinese)
- 849 Kaltenböck, R., Diendorfer, G., & Dotzek, N. (2009). Evaluation of thunderstorm
850 indices from ECMWF analyses, lightning data and severe storm reports.
851 *Atmospheric Research*, 93(1), 381–396. [https://doi.org/10.1016/](https://doi.org/10.1016/j.atmosres.2008.11.005)
852 [j.atmosres.2008.11.005](https://doi.org/10.1016/j.atmosres.2008.11.005)
- 853 Kanungo, T., Mount, D. M., Netanyahu, N. S., Piatko, C. D., Silverman, R., & Wu, A. Y.
854 (2002). An efficient k-means clustering algorithm: analysis and implementation.
855 *IEEE Transactions on Pattern Analysis and Machine Intelligence*, 24(7), 881–892.
856 <https://doi.org/10.1109/TPAMI.2002.1017616>
- 857 King, A. T., & Kennedy, A. D. (2019). North American supercell environments in
858 atmospheric reanalyses and RUC-2. *Journal of Applied Meteorology and*
859 *Climatology*, 58(1), 71–92. <https://doi.org/10.1175/JAMC-D-18-0015.1>

- 860 Kirkpatrick, J. C., McCaul, E. W., & Cohen, C. (2007). The motion of simulated
861 convective storms as a function of basic environmental parameters. *Monthly*
862 *Weather Review*, 135(9), 3033–3051. <https://doi.org/10.1175/MWR3447.1>
- 863 Kirkpatrick, J. C., McCaul, E. W., & Cohen, C. (2009). Variability of updraft and
864 downdraft characteristics in a large parameter space study of convective storms.
865 *Monthly Weather Review*, 137(5), 1550–1561. [https://doi.org/10.1175/](https://doi.org/10.1175/2008MWR2703.1)
866 [2008MWR2703.1](https://doi.org/10.1175/2008MWR2703.1)
- 867 Kirkpatrick, J. C., McCaul, E. W., & Cohen, C. (2011). Sensitivities of simulated
868 convective storms to environmental CAPE. *Monthly Weather Review*, 139(11),
869 3514–3532. <https://doi.org/10.1175/2011MWR3631.1>
- 870 Kolios, S., & Feidas, H. (2010). A warm season climatology of mesoscale convective
871 systems in the Mediterranean basin using satellite data. *Theoretical and Applied*
872 *Climatology*, 102(1–2), 29–42. <https://doi.org/10.1007/s00704-009-0241-7>
- 873 Ku, H.-Y., Noh, N., Jeong, J.-H., Koo, J.-H., Choi, W., Kim, B.-M., et al. (2021).
874 Classification of large-scale circulation patterns and their spatio-temporal
875 variability during High-PM10 events over the Korean Peninsula. *Atmospheric*
876 *Environment*, 262, 118632. <https://doi.org/10.1016/j.atmosenv.2021.118632>
- 877 Kubota, H., & Nitta, T. (2001). Diurnal variations of tropical convection observed
878 during the TOGA-COARE. *Journal of the Meteorological Society of Japan. Ser. II*,
879 79(3), 815–830. <https://doi.org/10.2151/jmsj.79.815>
- 880 Kuchera, E. L., & Parker, M. D. (2006). Severe convective wind environments. *Weather*
881 *and Forecasting*, 21(4), 595–612. <https://doi.org/10.1175/WAF931.1>
- 882 Kukulies, J., Chen, D., & Curio, J. (2021). The role of mesoscale convective systems in
883 precipitation in the Tibetan Plateau region. *Journal of Geophysical Research:*
884 *Atmospheres*, 126(23), e2021JD035279. <https://doi.org/10.1029/2021JD035279>
- 885 Laing, A. G., & Michael Fritsch, J. (1997). The global population of mesoscale
886 convective complexes. *Quarterly Journal of the Royal Meteorological Society*,
887 123(538), 389–405. <https://doi.org/10.1002/qj.49712353807>

- 888 Lewis, M. W., & Gray, S. L. (2010). Categorisation of synoptic environments
889 associated with mesoscale convective systems over the UK. *Atmospheric Research*,
890 97(1–2), 194–213. <https://doi.org/10.1016/j.atmosres.2010.04.001>
- 891 Li, J., Yu, R., Zhou, T., & Wang, B. (2005). Why is there an early spring cooling shift
892 downstream of the Tibetan Plateau? *Journal of Climate*, 18(22), 4660–4668.
893 <https://doi.org/10.1175/JCLI3568.1>
- 894 Li, X., Zhou, W., Chen, D., Li, C., & Song, J. (2014). Water vapor transport and
895 moisture budget over eastern China: remote forcing from the two types of El Niño.
896 *Journal of Climate*, 27(23), 8778–8792.
897 <https://doi.org/10.1175/JCLI-D-14-00049.1>
- 898 Li, Y., Wang, Y., Yang, S., Hu, L., Gao, S., & Fu, R. (2008). Characteristics of summer
899 convective systems initiated over the Tibetan Plateau. Part I: origin, track,
900 development, and precipitation. *Journal of Applied Meteorology and Climatology*,
901 47(10), 2679–2695. <https://doi.org/10.1175/2008JAMC1695.1>
- 902 Lin, X., Randall, D. A., & Fowler, L. D. (2000). Diurnal variability of the hydrologic
903 cycle and radiative fluxes: comparisons between observations and a GCM. *Journal*
904 *of Climate*, 13(23), 4159–4179. [https://doi.org/10.1175/1520-0442\(2000\)](https://doi.org/10.1175/1520-0442(2000)013<4159:DVOTHC>2.0.CO;2)
905 [013<4159:DVOTHC>2.0.CO;2](https://doi.org/10.1175/1520-0442(2000)013<4159:DVOTHC>2.0.CO;2)
- 906 Liu, N., Zhou, S., Liu, C., & Guo, J. (2019). Synoptic circulation pattern and boundary
907 layer structure associated with PM_{2.5} during wintertime haze pollution episodes in
908 Shanghai. *Atmospheric Research*, 228, 186–195.
909 <https://doi.org/10.1016/j.atmosres.2019.06.001>
- 910 Lu, X., Yu, H., Ying, M., Zhao, B., Zhang, S., Lin, L., et al. (2021). Western North
911 Pacific tropical cyclone database created by the China Meteorological
912 Administration. *Advances in Atmospheric Sciences*, 38(4), 690–699.
913 <https://doi.org/10.1007/s00376-020-0211-7>
- 914 Luo, Y., Wu, M., Ren, F., Li, J., & Wong, W.-K. (2016). Synoptic situations of extreme
915 hourly precipitation over China. *Journal of Climate*, 29(24), 8703–8719.
916 <https://doi.org/10.1175/JCLI-D-16-0057.1>

- 917 Ma, R., Sun, J., & Yang, X. (2021a). A 7-yr climatology of the initiation, decay, and
918 morphology of severe convective storms during the warm season over North China.
919 *Monthly Weather Review*, 149(8), 2599–2612.
920 <https://doi.org/10.1175/MWR-D-20-0087.1>
- 921 Ma, R., Sun, J., & Yang, X. (2021b). An eight-year climatology of the warm-season
922 severe thunderstorm environments over North China. *Atmospheric Research*, 254,
923 105519. <https://doi.org/10.1016/j.atmosres.2021.105519>
- 924 Machado, L. A. T., Rossow, W. B., Guedes, R. L., & Walker, A. W. (1998). Life cycle
925 variations of mesoscale convective systems over the Americas. *Monthly Weather*
926 *Review*, 126(6), 1630–1654. [https://doi.org/10.1175/1520-0493\(1998\)126<1630:](https://doi.org/10.1175/1520-0493(1998)126<1630:LCVOMC>2.0.CO;2)
927 [LCVOMC>2.0.CO;2](https://doi.org/10.1175/1520-0493(1998)126<1630:LCVOMC>2.0.CO;2)
- 928 Maddox, R. A. (1980). Mesoscale convective complexes. *Bulletin of the American*
929 *Meteorological Society*, 61(11), 1374–1400.
930 [https://doi.org/10.1175/1520-0477\(1980\)061<1374:MCC>2.0.CO;2](https://doi.org/10.1175/1520-0477(1980)061<1374:MCC>2.0.CO;2)
- 931 Mai Z., Fu, S., & Sun, J. (2020). Statistical features of two types of mesoscale
932 convective systems (MCSs) generated over the eastern Tibetan Plateau during 16
933 consecutive warm seasons. *Climatic and Environmental Research*, 25(4), 385–398,
934 <http://doi.org/10.3878/j.issn.1006-9585.2019.19040>. (in Chinese)
- 935 Marzban, C., & Sandgathe, S. (2010). Optical flow for verification. *Weather and*
936 *Forecasting*, 25(5), 1479–1494. <https://doi.org/10.1175/2010WAF2222351.1>
- 937 McCaul, E. W., & Weisman, M. L. (2001). The sensitivity of simulated supercell
938 structure and intensity to variations in the shapes of environmental buoyancy and
939 shear profiles. *Monthly Weather Review*, 129(4), 664–687. [https://doi.org/10.1175/](https://doi.org/10.1175/1520-0493(2001)129<0664:TSOSSS>2.0.CO;2)
940 [1520-0493\(2001\)129<0664:TSOSSS>2.0.CO;2](https://doi.org/10.1175/1520-0493(2001)129<0664:TSOSSS>2.0.CO;2)
- 941 Mecikalski, J. R., & Bedka, K. M. (2006). Forecasting convective initiation by
942 monitoring the evolution of moving cumulus in daytime GOES imagery. *Monthly*
943 *Weather Review*, 134(1), 49–78. <https://doi.org/10.1175/MWR3062.1>
- 944 Meng, Y., Sun, J., Zhang, Y., & Fu, S. (2021). A 10-year climatology of mesoscale

convective systems and their synoptic circulations in the southwest mountain area of China. *Journal of Hydrometeorology*, 22(1), 23–41. <https://doi.org/10.1175/JHM-D-20-0167.1>

Miao, Y., Guo, J., Liu, S., Liu, H., Li, Z., Zhang, W., & Zhai, P. (2017). Classification of summertime synoptic patterns in Beijing and their associations with boundary layer structure affecting aerosol pollution. *Atmospheric Chemistry and Physics*, 17(4), 3097–3110. <https://doi.org/10.5194/acp-17-3097-2017>

Miller, D., & Fritsch, J. M. (1991). Mesoscale convective complexes in the western Pacific region. *Monthly Weather Review*, 119(12), 2978–2992. [https://doi.org/10.1175/1520-0493\(1991\)119<2978:MCCITW>2.0.CO;2](https://doi.org/10.1175/1520-0493(1991)119<2978:MCCITW>2.0.CO;2)

Morake, D. M., Blamey, R. C., & Reason, C. J. C. (2021). Long-lived mesoscale convective systems over eastern South Africa. *Journal of Climate*, 1(aop), 1–66. <https://doi.org/10.1175/JCLI-D-20-0851.1>

Morel, C., & Senesi, S. (2002). A climatology of mesoscale convective systems over Europe using satellite infrared imagery. I: Methodology. *Quarterly Journal of the Royal Meteorological Society*, 128(584), 1953–1971. <https://doi.org/10.1256/003590002320603485>

Nga, P. T. T., Ha, P. T., & Hang, V. T. (2021). Satellite-based regionalization of solar irradiation in Vietnam by k-Means clustering. *Journal of Applied Meteorology and Climatology*, 60(3), 391–402. <https://doi.org/10.1175/JAMC-D-20-0070.1>

Ning, G., Yim, S. H. L., Yang, Y., Gu, Y., & Dong, G. (2020). Modulations of synoptic and climatic changes on ozone pollution and its health risks in mountain-basin areas. *Atmospheric Environment*, 240, 117808. <https://doi.org/10.1016/j.atmosenv.2020.117808>

Panosetti, D., Böing, S., Schlemmer, L., & Schmidli, J. (2016). Idealized large-eddy and convection-resolving simulations of moist convection over mountainous terrain. *Journal of the Atmospheric Sciences*, 73(10), 4021–4041. <https://doi.org/10.1175/JAS-D-15-0341.1>

Peters, J. M., & Schumacher, R. S. (2014). Objective categorization of

974 heavy-rain-producing MCS synoptic types by rotated principal component analysis.
 975 *Monthly Weather Review*, 142(5), 1716–1737.
 976 <https://doi.org/10.1175/MWR-D-13-00295.1>

977 Punkka, A.-J., & Bister, M. (2015). Mesoscale convective systems and their
 978 synoptic-scale environment in Finland. *Weather and Forecasting*, 30(1), 182–196.
 979 <https://doi.org/10.1175/WAF-D-13-00146.1>

980 Rasmussen, E. N., & Blanchard, D. O. (1998). A baseline climatology of
 981 sounding-derived supercell and tornado forecast parameters. *Weather and*
 982 *Forecasting*, 13(4), 1148–1164.
 983 [https://doi.org/10.1175/1520-0434\(1998\)013<1148:ABCOSD>2.0.CO;2](https://doi.org/10.1175/1520-0434(1998)013<1148:ABCOSD>2.0.CO;2)

984 Rehbein, A., Ambrizzi, T., & Mechoso, C. R. (2018). Mesoscale convective systems
 985 over the Amazon basin. Part I: climatological aspects. *International Journal of*
 986 *Climatology*, 38(1), 215–229. <https://doi.org/10.1002/joc.5171>

987 Reif, D. W., & Bluestein, H. B. (2017). A 20-year climatology of nocturnal convection
 988 initiation over the central and southern Great Plains during the warm season.
 989 *Monthly Weather Review*, 145(5), 1615–1639.
 990 <https://doi.org/10.1175/MWR-D-16-0340.1>

991 Roberts, R. D., & Rutledge, S. (2003). Nowcasting storm initiation and growth using
 992 GOES-8 and WSR-88D data. *Weather and Forecasting*, 18(4), 562–584.
 993 [https://doi.org/10.1175/1520-0434\(2003\)018<0562:NSIAGU>2.0.CO;2](https://doi.org/10.1175/1520-0434(2003)018<0562:NSIAGU>2.0.CO;2)

994 Rodgers, D. M., Howard, K. W., & Johnston, E. C. (1983). Mesoscale convective
 995 complexes over the United States during 1982. *Monthly Weather Review*, 111(12),
 996 2363–2369. [https://doi.org/10.1175/1520-0493\(1983\)111<2363:MCCOTU>2.0.CO;2](https://doi.org/10.1175/1520-0493(1983)111<2363:MCCOTU>2.0.CO;2)
 997 [https://doi.org/10.1175/1520-0493\(1983\)111<2363:MCCOTU>2.0.CO;2](https://doi.org/10.1175/1520-0493(1983)111<2363:MCCOTU>2.0.CO;2)

998 Rodgers, E. B., Chang, S. W., Stout, J., Steranka, J., & Shi, J.-J. (1991). Satellite
 999 observations of variations in tropical cyclone convection caused by
 1000 upper-tropospheric troughs. *Journal of Applied Meteorology and Climatology*,
 1001 30(8), 1163–1184. [https://doi.org/10.1175/1520-0450\(1991\)030<1163:SOOVIT>](https://doi.org/10.1175/1520-0450(1991)030<1163:SOOVIT>2.0.CO;2)
 1002 [2.0.CO;2](https://doi.org/10.1175/1520-0450(1991)030<1163:SOOVIT>2.0.CO;2)

- 1003 Rousseeuw, P. J. (1987). Silhouettes: A graphical aid to the interpretation and validation
1004 of cluster analysis. *Journal of Computational and Applied Mathematics*, 20, 53–65.
1005 [https://doi.org/10.1016/0377-0427\(87\)90125-7](https://doi.org/10.1016/0377-0427(87)90125-7)
- 1006 Shen, Y., Du, Y., & Chen, G. (2020). Ensemble sensitivity analysis of heavy rainfall
1007 associated with three MCSs coexisting over southern China. *Journal of*
1008 *Geophysical Research: Atmospheres*, 125(2). [https://doi.org/10.1029/](https://doi.org/10.1029/2019JD031266)
1009 [2019JD031266](https://doi.org/10.1029/2019JD031266)
- 1010 Shi, Y., Jiang, Z., Liu, Z., & Li, L. (2020). A Lagrangian analysis of water vapor sources
1011 and pathways for precipitation in East China in different stages of the east Asian
1012 summer monsoon. *Journal of Climate*, 33(3), 977–992. [https://doi.org/10.1175/](https://doi.org/10.1175/JCLI-D-19-0089.1)
1013 [JCLI-D-19-0089.1](https://doi.org/10.1175/JCLI-D-19-0089.1)
- 1014 Sieglaff, J. M., Counce, L. M., Feltz, W. F., Bedka, K. M., Pavolonis, M. J., & Heidinger,
1015 A. K. (2011). Nowcasting convective storm initiation using satellite-based
1016 box-averaged cloud-top cooling and cloud-type trends. *Journal of Applied*
1017 *Meteorology and Climatology*, 50(1), 110–126.
1018 <https://doi.org/10.1175/2010JAMC2496.1>
- 1019 Solman, S. A., & Menéndez, C. G. (2003). Weather regimes in the South American
1020 sector and neighbouring oceans during winter. *Climate Dynamics*, 21(1), 91–104.
1021 <https://doi.org/10.1007/s00382-003-0320-x>
- 1022 Song, F., Feng, Z., Leung, L. R., Jr, R. A. H., Wang, J., Hardin, J., & Homeyer, C. R.
1023 (2019). Contrasting spring and summer large-scale environments associated with
1024 mesoscale convective systems over the U.S. Great Plains. *Journal of Climate*,
1025 32(20), 6749–6767. <https://doi.org/10.1175/JCLI-D-18-0839.1>
- 1026 Stahl, K., Moore, R. D., & Mckendry, I. G. (2006). The role of synoptic-scale
1027 circulation in the linkage between large-scale ocean–atmosphere indices and winter
1028 surface climate in British Columbia, Canada. *International Journal of Climatology*,
1029 26(4), 541–560. <https://doi.org/10.1002/joc.1268>
- 1030 Sugimoto, S., & Ueno, K. (2010). Formation of mesoscale convective systems over the
1031 eastern Tibetan Plateau affected by plateau-scale heating contrasts. *Journal of*

- 1032 *Geophysical Research: Atmospheres*, 115. <https://doi.org/10.1029/2009JD013609>
- 1033 Sun, J., & Zhang, F. (2012). Impacts of mountain–plains solenoid on diurnal variations
1034 of rainfalls along the mei-yu front over the East China plains. *Monthly Weather*
1035 *Review*, 140(2), 379–397. <https://doi.org/10.1175/MWR-D-11-00041.1>
- 1036 Sun J., Wei J., Fu S., Zhang Y. & Wang H., 2018: The multi-scale physical model for
1037 persistent heavy rainfall events in the Yangtze-Huaihe River valley. *Chinese*
1038 *Journal of Atmospheric Sciences*, 42(4), 741–754,
1039 <http://doi.org/10.3878/j.issn.1006-9895.1803.17246>. (in Chinese)
- 1040 Tao, S. (1980). *Heavy Rainfalls in China*. Beijing: Science Press.
- 1041 Ternynck, C., Alaya, M. A. B., Chebana, F., Dabo-Niang, S., & Ouarda, T. B. M. J.
1042 (2016). Streamflow hydrograph classification using functional data analysis.
1043 *Journal of Hydrometeorology*, 17(1), 327–344.
1044 <https://doi.org/10.1175/JHM-D-14-0200.1>
- 1045 Vandal, T., & Nemani, R. (2020). Temporal interpolation of geostationary satellite
1046 imagery with task specific optical flow. *Proceedings of 1st ACM SIGKDD*
1047 *Workshop on Deep Learning for Spatiotemporal Data, Applications, and Systems*
1048 *(DeepSpatial '20)*, 9 pp. [http://mason.gmu.edu/~lzhao9/venues/DeepSpatial2020/](http://mason.gmu.edu/~lzhao9/venues/DeepSpatial2020/papers/DeepSpatial_paper_6_camera_ready.pdf)
1049 [papers/DeepSpatial_paper_6_camera_ready.pdf](http://mason.gmu.edu/~lzhao9/venues/DeepSpatial2020/papers/DeepSpatial_paper_6_camera_ready.pdf)
- 1050 Velasco, I., & Fritsch, J. M. (1987). Mesoscale convective complexes in the Americas.
1051 *Journal of Geophysical Research: Atmospheres*, 92(D8), 9591–9613.
1052 <https://doi.org/10.1029/JD092iD08p09591>
- 1053 Wang, H., Sun, J., Fu, S., & Zhang, Y. (2021). Typical circulation patterns and
1054 associated mechanisms for persistent heavy rainfall events over Yangtze-Huaihe
1055 River Valley during 1981–2020. *Advances in Atmospheric Sciences*, 38(12), 2167–
1056 2182. <https://doi.org/10.1007/s00376-021-1194-8>
- 1057 Williams, M., & Houze, R. A. (1987). Satellite-observed characteristics of winter
1058 monsoon cloud clusters. *Monthly Weather Review*, 115(2), 505–519.
1059 [https://doi.org/10.1175/1520-0493\(1987\)115<0505:SOCOWM>2.0.CO;2](https://doi.org/10.1175/1520-0493(1987)115<0505:SOCOWM>2.0.CO;2)

- 1060 Wilson, J. W., & Roberts, R. D. (2006). Summary of convective storm initiation and
1061 evolution during IHOP: observational and modeling perspective. *Monthly Weather*
1062 *Review*, 134(1), 23–47. <https://doi.org/10.1175/MWR3069.1>
- 1063 Yang, J., Zhang, Z., Wei, C., Lu, F., & Guo, Q. (2017). Introducing the new generation
1064 of Chinese geostationary weather satellites, Fengyun-4. *Bulletin of the American*
1065 *Meteorological Society*, 98(8), 1637–1658.
1066 <https://doi.org/10.1175/BAMS-D-16-0065.1>
- 1067 Yang, J., Zhao, K., Chen, X., Huang, A., Zheng, Y., & Sun, K. (2020). Subseasonal and
1068 diurnal variability in lightning and storm activity over the Yangtze River Delta,
1069 China, during mei-yu season. *Journal of Climate*, 33(12), 5013–5033.
1070 <https://doi.org/10.1175/JCLI-D-19-0453.1>
- 1071 Yang, R., Zhang, Y., Sun, J., & Li, J. (2020). The comparison of statistical features and
1072 synoptic circulations between the eastward-propagating and quasi-stationary MCSs
1073 during the warm season around the second-step terrain along the middle reaches of
1074 the Yangtze River. *Science China Earth Sciences*, 63(8), 1209–1222.
1075 <https://doi.org/10.1007/s11430-018-9385-3>
- 1076 Yang, X., Fei, J., Huang, X., Cheng, X., Carvalho, L. M. V., & He, H. (2015).
1077 Characteristics of mesoscale convective systems over China and its vicinity using
1078 geostationary satellite FY2. *Journal of Climate*, 28(12), 4890–4907.
1079 <https://doi.org/10.1175/JCLI-D-14-00491.1>
- 1080 Yang, X., & Sun, J. (2018). Organizational modes of severe wind-producing convective
1081 systems over North China. *Advances in Atmospheric Sciences*, 35(5), 540–549.
1082 <https://doi.org/10.1007/s00376-017-7114-2>
- 1083 Yang, Y., Wang, R., Chen, F., Liu, C., Bi, X., & Huang, M. (2021). Synoptic weather
1084 patterns modulate the frequency, type and vertical structure of summer precipitation
1085 over Eastern China: a perspective from GPM observations. *Atmospheric Research*,
1086 249, 105342. <https://doi.org/10.1016/j.atmosres.2020.105342>
- 1087 Ying, M., Zhang, W., Yu, H., Lu, X., Feng, J., Fan, Y., et al. (2014). An overview of the
1088 China Meteorological Administration tropical cyclone database. *Journal of*

- 1089 *Atmospheric and Oceanic Technology*, 31(2), 287–301.
1090 <https://doi.org/10.1175/JTECH-D-12-00119.1>
- 1091 Yu, R., Zhou, T., Xiong, A., Zhu, Y., & Li, J. (2007). Diurnal variations of summer
1092 precipitation over contiguous China. *Geophysical Research Letters*, 34(1).
1093 <https://doi.org/10.1029/2006GL028129>
- 1094 Zhang, A. Q., Chen, Y. L., Zhou, S. N., Cui, C. G., Wan, R., & Fu, Y. F. (2020). Diurnal
1095 variation of meiyu rainfall in the Yangtze Plain during atypical meiyu years.
1096 *Journal of Geophysical Research: Atmospheres*, 125(1), e2019JD031742.
1097 <https://doi.org/10.1029/2019JD031742>
- 1098 Zhang, X., Shen, W., Zhuge, X., Yang, S., Chen, Y., Wang, Y., Chen, T., & Zhang, S.
1099 (2021). Statistical characteristics of mesoscale convective systems initiated over the
1100 Tibetan Plateau in summer by Fengyun satellite and precipitation estimates. *Remote*
1101 *Sensing*, 13(9). <https://doi.org/10.3390/rs13091652>
- 1102 Zhang, X., Wang, X. L., & Corte-Real, J. (1997). On the relationships between daily
1103 circulation patterns and precipitation in Portugal. *Journal of Geophysical Research:*
1104 *Atmospheres*, 102(D12), 13495–13507. <https://doi.org/10.1029/97JD01012>
- 1105 Zhang, Y., & Sun, J. (2017). Comparison of the diurnal variations of precipitation east
1106 of the Tibetan Plateau among sub-periods of Meiyu season. *Meteorology and*
1107 *Atmospheric Physics*, 129(5), 539–554.
1108 <https://doi.org/10.1007/s00703-016-0484-7>
- 1109 Zhang, Y., Zhang, F., & Sun, J. (2014). Comparison of the diurnal variations of
1110 warm-season precipitation for East Asia vs. North America downstream of the
1111 Tibetan Plateau vs. the Rocky Mountains. *Atmospheric Chemistry and Physics*,
1112 14(19), 10741–10759. <https://doi.org/10.5194/acp-14-10741-2014>
- 1113 Zhang, Y., Zhang, F., Davis, C. A., & Sun, J. (2018). Diurnal evolution and structure of
1114 long-lived mesoscale convective vortices along the mei-yu front over the East
1115 China plains. *Journal of the Atmospheric Sciences*, 75(3), 1005–1025.
1116 <https://doi.org/10.1175/JAS-D-17-0197.1>
- 1117 Zheng, L., Sun, J., Zhang, X., & Liu, C. (2013). Organizational modes of mesoscale

- 1118 convective systems over Central East China. *Weather and Forecasting*, 28(5),
1119 1081–1098. <https://doi.org/10.1175/WAF-D-12-00088.1>
- 1120 Zheng, Y., Chen, J., & Zhu, P. (2008). Climatological distribution and diurnal variation
1121 of mesoscale convective systems over China and its vicinity during summer.
1122 *Chinese Science Bulletin*, 53(10), 1574–1586.
1123 <https://doi.org/10.1007/s11434-008-0116-9>
- 1124 Zhu, L., Liu, J., Zhu, A., Sheng, M., & Duan, Z. (2018). Spatial distribution of diurnal
1125 rainfall variation in summer over China. *Journal of Hydrometeorology*, 19(4), 667–
1126 678. <https://doi.org/10.1175/JHM-D-17-0176.1>
- 1127 Zipser, E. J. (1977). Mesoscale and convective-scale downdrafts as distinct
1128 components of squall-line structure. *Monthly Weather Review*, 105(12), 1568–1589.
1129 [https://doi.org/10.1175/1520-0493\(1977\)105<1568:MACDAD>2.0.CO;2](https://doi.org/10.1175/1520-0493(1977)105<1568:MACDAD>2.0.CO;2)